ADVANCING EARTH AND SPACE SCIENCE

Geochemistry, Geophysics, Geosystems

RESEARCH ARTICLE
10.1029/2020GC009485

Key Points:

- New ages of basalts from the Macquarie Ridge Complex (MRC) at the Australia-Pacific plate boundary are reported
- The cessation of seafloor spreading was progressed from south to north along the Macquarie Ridge
- Upper mantle heterogeneity becomes obvious at dying mid-ocean ridges where the melting degrees are low and various melt compositions are produced

Supporting Information:

- Supporting Information S1
- Table S1
- Table S2
- Table S3
- Table S4
- Figure S1

Correspondence to:

Q. Jiang,
qiang.jiang1@postgrad.curtin.edu.au

Citation:

Jiang, Q., Merle, R. E., Jourdan, F., Olierook, H. K.H., Whitehouse, M. J., Evans, K. A., et al. (2021). Timing of seafloor spreading cessation at the Macquarie Ridge Complex (SW Pacific) and implications for upper mantle heterogeneity. *Geochemistry, Geophysics, Geosystems*, *22*, e2020GC009485. https://doi.org/10.1029/2020GC009485

Received 19 OCT 2020
Accepted 16 DEC 2020

Timing of Seafloor Spreading Cessation at the Macquarie Ridge Complex (SW Pacific) and Implications for Upper Mantle Heterogeneity

Qiang Jiang[1,2], Renaud E. Merle[3,4], Fred Jourdan[1,2], Hugo K.H. Olierook[2,5], Martin J. Whitehouse[3], Katy A. Evans[2], Xuan-Ce Wang[6], Chris E. Conway[7], Helen C. Bostock[8], and Richard J. Wysoczanski[9]

[1]Western Australian Argon Isotope Facility & John de Laeter Centre, Perth, WA, Australia, [2]School of Earth and Planetary Sciences, Curtin University, Perth, WA, Australia, [3]Swedish Museum of Natural History, Stockholm, Sweden, [4]Department of Earth Sciences, Natural Resources and Sustainable Development, Uppsala University, Uppsala, Sweden, [5]Timescales of Mineral Systems, Centre for Exploration Targeting – Curtin Node, Curtin University, Perth, WA, Australia, [6]School of Geoscience, Yunnan University, Kunming, China, [7]Institute of Earthquake and Volcano Geology, Geological Survey of Japan, AIST, Central 7, Ibaraki, Tsukuba, Japan, [8]School of Earth and Environmental Sciences, The University of Queensland, Brisbane, QLD, Australia, [9]National Institute of Water and Atmospheric Research, Wellington, New Zealand

Abstract The Macquarie Ridge Complex (MRC) on the Australia-Pacific plate boundary south of New Zealand is an extinct mid-ocean ridge that has experienced a complex tectonic history and produced highly heterogeneous mid-ocean ridge basalts (MORBs). When and how seafloor spreading ceased along the proto-Macquarie mid-ocean ridge remain elusive, and it is unclear how the mantle source of MORBs is affected by the gradual cessation of seafloor spreading at mid-ocean ridges. To constrain the tectonic evolution of the MRC, the mantle source variations for MORBs at dying mid-ocean ridges, and the mechanisms of mantle enrichment and asthenospheric heterogeneities, we report 11 pyroxene, plagioclase, basaltic glass, groundmass, and sericite ^{40}Ar/^{39}Ar and one zircon U-Pb ages for the MRC MORBs. Our data reveal that basalts from the MRC seamounts were erupted between 25.9 and 1.6 Ma and Macquarie Island at ~10 Ma. Combined age and plate reconstruction results reveal that the cessation of seafloor spreading at the MRC generally propagated from south to north along the ridge. Basalts produced by the then dying Macquarie mid-ocean ridge at different times on different seamounts/island show a large variation in isotopic compositions and there is no clear correlation between ages and isotopic ratios. The heterogeneity of mantle source for MORBs from the proto-Macquarie mid-ocean ridge suggests that the upper asthenospheric mantle is heterogeneous, and such heterogeneity becomes most obvious at dying mid-ocean ridges where the degrees of partial melting are low and a large range of melt compositions are produced.

1. Introduction

Mid-ocean ridges are Earth's most important producers of igneous rocks and contribute ~75% of Earth's present-day volcanism (Crisp, 1984). While much is known about the production of mid-ocean ridge basalts (MORBs) by mantle upwelling and decompression melting at active mid-ocean ridges, the magmatic processes during mid-ocean ridges' slowdown and eventual cessation in response to plate reorganization are less well understood. Despite, the wide distribution of extinct mid-ocean ridges on Earth (see review of MacLeod et al., 2017), much of current knowledge of such processes comes from studies of the fossil Phoenix Ridge off the Antarctic Peninsula (Choe et al., 2007; Choi et al., 2008; Choi et al., 2013; Haase et al., 2011b), the Galapagos Rise fossil ridge (Haase et al., 2011a), and the Mathematician Ridge, Gorda Ridge, and other fossil ridge segments off the California coastline (Batiza & Vanko, 1985; Castillo et al., 2010; Davis et al., 2008, 2010; Tian et al., 2011). At the Australian–Pacific plate boundary south of New Zealand, the ~1,600 km-long Macquarie Ridge Complex (MRC) is a much longer but poorly documented extinct mid-ocean ridge system. Compared with the aforementioned fossil mid-ocean ridges, the MRC experienced more complex tectonic processes which transitioned from a spreading axis to a transform plate boundary since ~30 Ma (e.g., Massell et al., 2000; Mosher & Symons, 2008), and therefore can yield further insights into the tectonic and magmatic processes during rapid transition at mid-ocean ridges (Figure 1a).

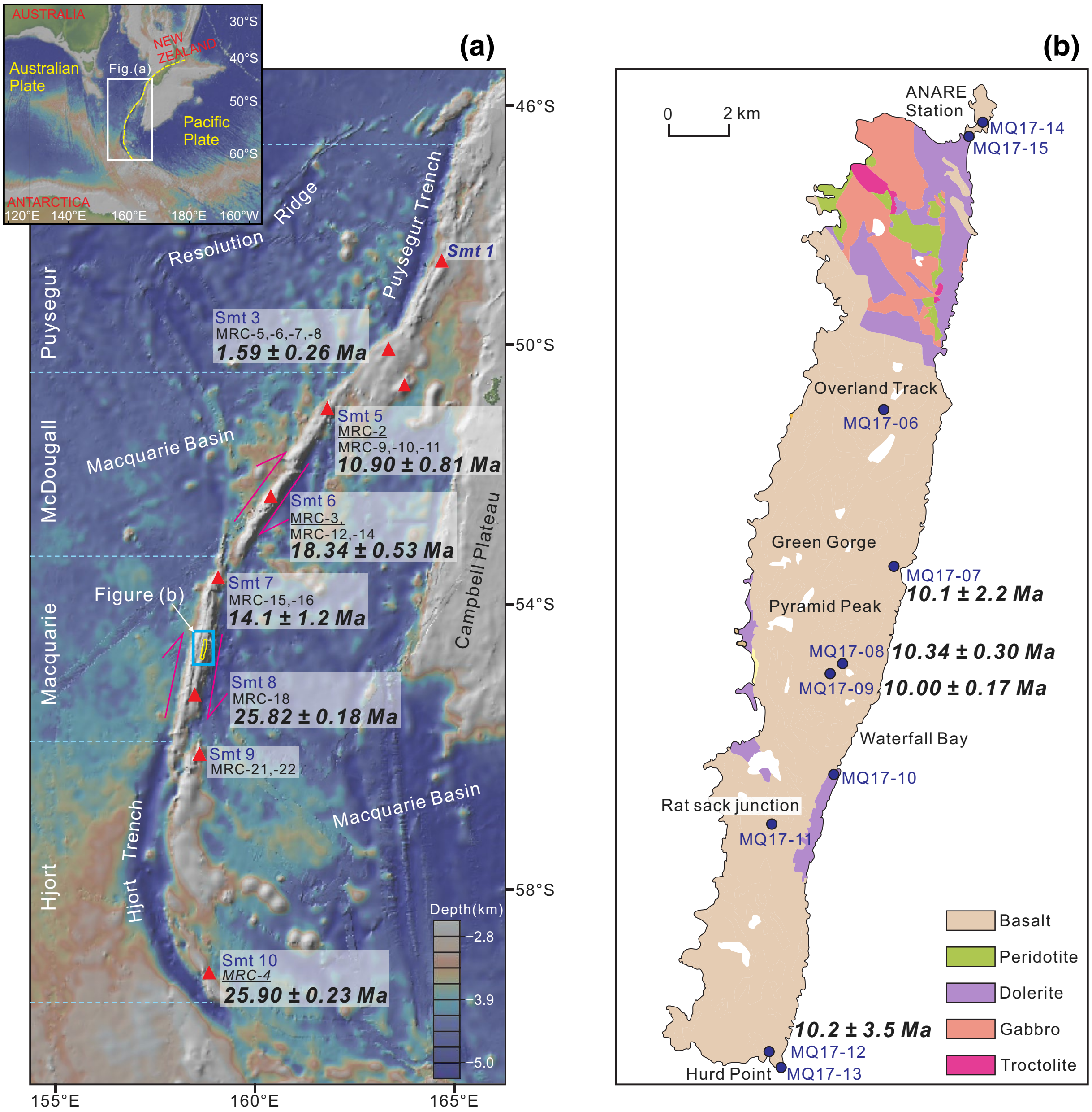

Figure 1. (a) Bathymetric map of the Macquarie Basin in SW Pacific, made using GeoMapApp (Ryan et al., 2009). Naming convention for the seamounts (marked by red triangles) is from Conway et al. (2012) based on original TAN0803 voyage report. The blue box indicates the location of Macquarie Island. Inset shows the location of the Macquarie Ridge Complex. The yellow solid line indicates the Australian-Pacific plate boundary. (b) Geological map of Macquarie Island, after Goscombe & Everard (1998). Sample locations and ages are annotated. The magenta arrows show the transform motions of the Macquarie Ridge Complex (MRC).

Geochemical and isotopic data for basalts from the MRC and other extinct mid-ocean ridges reveal a continuum from normal MORB (N-MORB) to transitional MORB to enriched MORB (E-MORB; Castillo et al., 2010; Choi et al., 2008; Jiang et al., 2020; Kamenetsky et al., 2000; Tian et al., 2011). The production of geochemically and isotopically varied magma by dying mid-ocean ridges has led to different hypotheses to account for the heterogeneity of the asthenospheric upper mantle and evolution of the mantle source at mid-ocean ridges. For example, some studies argue that volcanism at dying mid-ocean ridges evolves with time from N-MORB to E-MORB, as seafloor spreading transitioned from active, to slowdown and eventual cessation (Choe et al., 2007; Choi et al., 2008; Haase et al., 2011b; Tian et al., 2011). Alternatively, cyclic magmatic activity beneath mid-ocean ridges might produce E-MORB at the beginning of a magmatic pulse dominated by enriched mantle material, and N-MORB at the end of a cycle once enriched material is consumed (Choi et al., 2013).

Understanding the magmatic evolution and temporal variations of geochemical and isotopic characteristics of MORBs during the extinction of mid-ocean ridges necessitates a robust temporal context for these data. However, geochronological data are generally scarce for extinct mid-ocean ridges because minerals amenable to ^{40}Ar/^{39}Ar geochronology (e.g., plagioclase) are often altered in oceanic basaltic rocks (e.g., Merle et al., 2019) or contain excess ^{40}Ar and low K contents (Duncan & Hogan, 1994), and minerals suitable for U-Pb geochronology (e.g., zircon) are rare. For the MRC, a single study attempted to investigate the age of the only emergent part—Macquarie Island (Figure 1b)-via both K–Ar and ^{40}Ar/^{39}Ar dating, but yielded inconclusive crystallization ages for the basalts (Duncan & Varne, 1988). The youngest magnetic anomaly identified in the Macquarie Basin is Chron C7 (~24 Ma; Keller, 2004) but identification of magnetic anomalies in the vicinity of the MRC is difficult due to the closely spaced magnetic anomalies and curved fracture zones (Keller, 2004; Massell et al., 2000). Therefore, it remains unclear when seafloor spreading ceased and when the basalts on the MRC were produced.

The occurrence of fresh plagioclase, pyroxene and even rare zircon in some MRC samples presents opportunities to constrain the timing of magmatic activity along this ~1,600 km-long extinct mid-ocean ridge using high-precision ^{40}Ar/^{39}Ar and U-Pb geochronology. Here we present a systematic ^{40}Ar/^{39}Ar (n = 56) and U-Pb (n = 1) study of the geochronology of the MRC, including Macquarie Island. Oxygen isotopic signatures of zircon grains are also measured, to assess if the zircon crystals were mantle-derived. Combined with previously reported geochemical and isotopic data, we explore the evolution of the chemical characteristics of MORBs along the MRC through time, and discuss the implications for magmatic evolution of dying mid-ocean ridges.

2. Geological Setting

2.1. Tectonic Evolution of the Macquarie Ridge Complex

The MRC is a NNE-SSW trending extinct mid-ocean ridge located between South Island, New Zealand, and the Australian-Pacific-Antarctic triple junction (Figure 1a; Massell et al., 2000; Sutherland, 1995). From south to north, it was divided into four segments (Hjort, Macquarie, McDougall, and Puysegur) based on discontinuities and changes in orientation (Figure 1b; Massell et al., 2000). The MRC evolved from a seafloor-spreading ridge to a transform and convergent plate boundary over ~40 Ma. Specifically: (1) at ~42 Ma, the Macquarie Basin opened as the Campbell Plateau and Resolution Ridge separated. The oldest seafloor magnetic anomaly identified is Chron C18 and a slow-spreading rate of ~1.5 cm yr^{-1} was estimated between magnetic anomalies Chron C18 and C11 (~40–30 Ma; Wood et al., 1996). (2) Since ~30 Ma, changes in relative motion between the Pacific plate and Australian plate caused oblique spreading of the proto-Macquarie mid-ocean ridge relative to the plate boundary (Massell et al., 2000; Wood et al., 1996). To accommodate the changes in spreading direction, the ridge segments shortened and the fracture zones became curved (Mosher & Symons, 2008). The spreading rate during this period is poorly constrained due to a lack of magnetic anomaly data, but was believed to be slow to intermediate (Wertz, 2003). (3) Seafloor spreading and magmatism is thought to have ceased by ~6 Ma when the relative motions of the Australian and Pacific plates became too oblique to sustain extension (Mosher & Symons, 2008; Wertz, 2003). To accommodate the two plates' convergence, incipient oceanic-oceanic subduction occurred in the southern and northern segments (Hjort and Puysegur) and strike-slip motion in the central segments (McDougall and Macquarie, Figure 1a; Lebrun et al., 2003; Meckel et al., 2003; Meckel et al., 2005).

2.2. Geochemistry of the Macquarie Ridge MORBs

Rocks from the MRC seamounts and Macquarie Island are alkaline to sub-alkaline basalts with geochemical compositions ranging from N-MORB to E-MORB and isotopic compositions lying between the fields of MORBs from the Pacific-Antarctic Ridge and HIMU-like basalts (Conway et al., 2012; Jiang et al., 2020; Kamenetsky et al., 2000; Kamenetsky & Maas, 2002). The geochemical and isotopic compositions are highly heterogeneous for rocks from each individual seamount (Conway et al., 2012; Jiang et al., 2020), and Macquarie Island (Kamenetsky et al., 2000; Kamenetsky & Maas, 2002), and there is no systematic latitudinal variations along the MRC (Jiang et al., 2020). Such heterogeneous geochemical characteristics were interpreted to be unrelated to hotspot contamination, but were attributed to pyroxenite veins generated in the metasomatized upper mantle (Jiang et al., 2020). The large variations from depleted to enriched compositions of the MRC MORBs are similar to those of MORBs from the fossil Phoenix Ridge (Choi et al., 2008; Haase et al., 2011b), fossil spreading ridges off the California coastline (Castillo et al., 2010; Tian et al., 2011), and ultraslow-spreading ridges such as the Mohns Ridge (Haase et al., 1996; Neumann & Schilling, 1984).

3. Samples

3.1. Macquarie Ridge Complex Seamounts

Rock samples were dredged from the MRC seamounts during the USNS *Eltanin* Marine Geology Cruises 16 and 37 in the 1960s and an RV *Tangaroa* voyage (TAN0803) in 2008 (Conway et al., 2012). In the present study, we report plagioclase, pyroxene, hornblende, sericite and groundmass ^{40}Ar/^{39}Ar geochronology analytical results from 17 samples of seven seamounts (Figure 1a; naming convention from Conway et al. (2012) based on original TAN0803 voyage report). The dredged lithologies include basalt, gabbro, dolerite, and glassy breccia. We only chose basaltic rocks that were angular and showed no evidence of glacial transportation (e.g., striations).

The dated samples from the MRC seamounts are sparsely porphyritic and non-vesicular basalts, dolerite (MRC-4) and gabbro (MRC-11). In thin section (Figures 2 and S2), the groundmass of the basalts comprises glass and plagioclase microphenocrysts and the phenocrysts are represented by plagioclase and clinopyroxene from 0.1 to 3 mm in length. The dolerite and gabbro samples are holocrystalline and the mineral phases include plagioclase, pyroxene and hornblende.

3.2. Macquarie Island

Rocks exposed on Macquarie Island are mostly peridotites and lower crustal gabbros on the northern quarter of the island, and massive to tabular basaltic lavas and pillow lavas in the central and southern parts of the island (Figure 1b; Dijkstra et al., 2010; Goscombe & Everard, 1998; Kamenetsky et al., 2000; Varne et al., 2000). Samples analyzed for the present study were collected during an expedition to Macquarie Island in November 2017. The dated samples from Macquarie Island include basalt, dolerite, and gabbro. We report the ^{40}Ar/^{39}Ar ages of plagioclase, pyroxene, hornblende, glass, and groundmass, and zircon U–Pb ages, and oxygen isotopes from 10 basaltic samples. The basaltic rocks of Macquarie Island are mostly subalkaline basalts.

In thin section (Figures 2 and S2), the plagioclase phenocrysts of the basalts are subhedral to anhedral and 0.1–4 mm in length, and the groundmass comprises a mixture of microcrystalline plagioclase, pyroxene, Fe-Ti oxides, and olivine. The dolerite (MQ17-10, -11) and gabbro (MQ17-08) samples are medium- to coarse-grained and holocrystalline. The mineral phases include plagioclase, pyroxene, olivine and minor hornblende. The glassy breccia, MQ17-09, consists of glass (> 80 vol.%), olivine, hornblende, and pyroxene. The hornblende crystals are anhedral and commonly form rims on pyroxene grains, therefore they may not be primary and are not used for ^{40}Ar/^{39}Ar dating. Alteration minerals, such as sericite, zeolite, and chlorite are present in some of the samples (e.g., Figures 2a–2d).

4. Analytical Methods

4.1. ^{40}Ar/^{39}Ar Geochronology

The samples were crushed by a clean tungsten carbide hydraulic press and mill, and sieved to separate the 212–355 μm and 125–212 μm size fractions. These fractions were thoroughly rinsed with distilled water in an ultrasonic cleaner to remove dust or powder from the grains. Minerals were separated using a Frantz isodynamic magnetic separator. Unaltered, optically transparent, inclusion-free plagioclase, pyroxene, and glass grains were handpicked carefully grain-by-grain under a binocular microscope from the 125–212 μm or the 212–355 μm, non-magnetic (plagioclase) or low-magnetic (pyroxene and glass) fractions. Homogenous groundmass grains were handpicked from the magnetic fractions. Grains showing evidence of

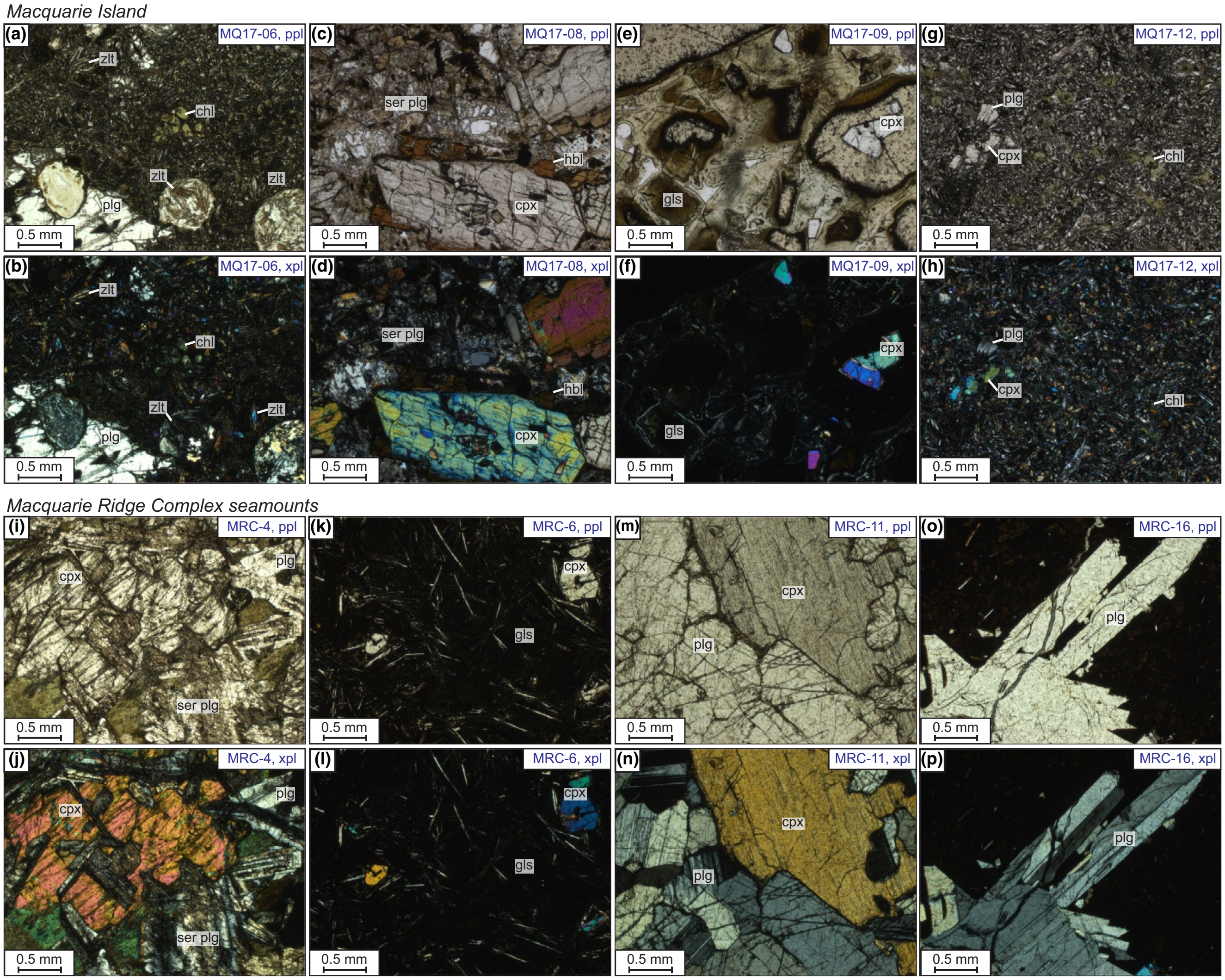

Figure 2. Representative thin section photomicrographs of samples from the Macquarie Ridge Complex. (a, b) Sample MQ17-06. (c, d) Sample MQ17-08. (e, f) Sample MQ17-09. (g, h) Sample MQ17-12. (i, j) Sample MRC-4. (k, l) Sample MRC-6. (m, n) Sample MRC-11. (o, p) Sample MRC-16. Chl, chlorite; cpx, clinopyroxene; gls, glass; hbl, hornblende; plg, plagioclase; ppl, plane polarized light; ser plg, sericitized; xpl, cross polarized light; zlt = zeolite.

alteration (e.g., brown, red or yellow discoloration) were avoided where possible, but cryptic alteration was difficult to detect because the groundmass is not transparent. The selected mineral and groundmass grains were leached in diluted (5 N) HF for 1 min and thoroughly rinsed in distilled water.

Multi-grain aliquots of the samples were loaded into several large wells, 1.9 cm diameter and 0.3 cm depth, within aluminum discs. A series of fully intercalibrated FC sanidine (Jourdan & Renne, 2007) and GA1550 biotite (Renne et al., 1998) standards, with ages of 28.294 ± 0.037 Ma and 99.738 ± 0.100 Ma (Renne et al., 2011), were loaded beside the samples in the same discs, which were irradiated for 3 h. The discs were Cd-shielded to minimize undesirable nuclear interference reactions and irradiated in the Oregon State University nuclear reactor (USA) in a central position. For each disc, an average *J*-value was computed from standard grains within the small pits, and was used in the age calculations of samples from pits surrounding those of the standards. The *J*-value of each sample is shown in Table S1. Mass discrimination was monitored regularly throughout the analysis using an automated air pipette, and mean values ranged from 0.987368 ± 0.03 to 0.99750 ± 0.05 ($\%1\sigma$) per Dalton (atomic mass unit) relative to an air ratio of 298.56 ± 0.31 (Lee et al., 2006). The correction factors for interfering isotopes were $(^{39}\mathrm{Ar}/^{37}\mathrm{Ar})_{\mathrm{Ca}} = 6.95 \times 10^{-4}$ (± 1.3%), $(^{36}\mathrm{Ar}/^{37}\mathrm{Ar})_{\mathrm{Ca}} = 2.65 \times 10^{-4}$ (± 0.84%) and $(^{40}\mathrm{Ar}/^{39}\mathrm{Ar})_{\mathrm{K}} = 7.30 \times 10^{-4}$ (± 12%; Renne et al., 2013). The most important correction value required for Ca-rich samples (e.g., plagioclase and pyroxene) is $(^{36}\mathrm{Ar}/^{37}\mathrm{Ar})_{\mathrm{Ca}}$.

This was re-measured in our laboratory in 2017 and yielded a value of $(^{36}Ar/^{37}Ar)_{Ca} = 2.65 \times 10^{-4}$ (± 1.6%), in agreement with the value measured by Renne et al. (2013). The $^{40}Ar/^{39}Ar$ analyses were performed at the Western Australian Argon Isotope Facility at Curtin University. Multi-grain aliquots of mineral crystals and groundmass were step-heated using a continuous 100 W PhotonMachine© CO_2 (IR, 10.4 μm) laser fired on the samples for 60 s. Each of the standard crystals was fused in a single step.

The gas was purified in an extra low-volume stainless steel extraction line of 240 cc volume, using one SAES AP10 and one GP50 getter. The Ar isotopes were measured in static mode using a low volume (600 cc) Thermofisher© ARGUS VI mass spectrometer set with a permanent resolution of ~200 (Jourdan et al., 2017). Measurements were performed in multi-collection mode using 4 Faraday cups with 10^{12} ohm resistors to measure masses of 40, 38, and 37 and a 10^{13} ohm resistor to measure mass 39. Mass 36 was measured using an ultralow background compact discrete dynode ion counter. We measured the relative abundance of each mass simultaneously using 10 cycles of peak-hopping and 16 s of integration time for each mass. Detectors were calibrated to each other electronically and using air shot beam signals. The raw data were processed using the ArArCALC software (Koppers, 2002) and the ages were calculated using the decay constants of Renne et al. (2011). Blanks were monitored every three to four steps. All parameters and relative abundance values are provided in Table S1 following the recommendations of Schaen et al. (2020), and corrected for blank, mass discrimination and radioactive decay.

Our criteria for the determination of a robust plateau age are as follows: (1) $^{40}Ar/^{39}Ar$ plateaus obtained from fresh mineral separates are preferred to those from groundmass; (2) $^{40}Ar/^{39}Ar$ plateaus must include at least 70% of the released ^{39}Ar (e.g., Olierook et al., 2019; Ware & Jourdan, 2018); (3) The plateaus should be defined by at least 3 consecutive steps consistent at 95% confidence level and satisfying a probability of fit (p) of at least 0.05; (4) $^{40}Ar/^{36}Ar$ intercepts should, ideally, overlap with the atmospheric $^{40}Ar/^{36}Ar$ ratio of 298.56 ± 0.31 (Lee et al., 2006). If the $^{40}Ar/^{36}Ar$ composition of the trapped argon measured for a statistically reliable $^{39}Ar/^{40}Ar$–$^{36}Ar/^{40}Ar$ isochron ($p > 0.05$) differs from an atmospheric value, then the measured ratio and its uncertainties are used in the age spectrum model age calculation, following the approach of Oostingh et al. (2017). Where robust mineral plateau ages are not available to constrain the age of the MRC seamount/island, relatively reliable ages that meet the following criteria are considered: (1) Mini-plateau (with 50%–70% ^{39}Ar released) ages obtained from mineral separates; (2) Plateau (with > 70% ^{39}Ar released) ages obtained from groundmass separates. We note that groundmass plateau ages should be treated with caution. This is because groundmass samples are prone to ^{39}Ar recoil loss (Jourdan et al., 2007; Renne et al., 2015) and/or K-leaching by hydrothermal alteration, which can lead to older apparent plateau ages. Furthermore, ^{40}Ar loss and/or recrystallization from cryptic hydrothermal alteration phases, which are much harder to detect visually in the groundmass than in mineral separates (Hofmann et al., 2000), especially for submarine basalts, produce younger apparent plateau ages. These effects are less problematic for rocks younger than ~30 Ma, because there is less chance that they are altered significantly, but even in this case, the age validity must be critically evaluated against alteration indicators such as optical petrography and the water content of the rock (loss-on-ignition, LOI); fresh basalts should have LOI values < 2 wt.%.

Plateau ages are given at the 2σ level and are calculated from the mean of all plateau steps, each weighted by the inverse variance of their individual analytical error. Preferred plateau ages with all sources of uncertainties calculated following the error propagation approach of Renne et al. (2010), based on Monte Carlo simulations and appropriate R-values and their uncertainties, are provided in Table 1.

4.2. Zircon Oxygen Isotopes and U–Pb Geochronology

We used a Tescan Integrated Mineral Analyzer (TIMA) to aid in mineral identification for the dolerite and gabbro samples from the MRC, and zircon grains were found in sample MRC-18 (Figure S5). To separate the zircon grains, the sample was crushed with a hydraulic press and in a clean tungsten carbide mill. A Wilfley concentrating shaker table and LST heavy liquids (2.9 g cm^{-3}) were used to concentrate the heavy minerals. The heavy fraction was run through a Frantz isodynamic magnetic separator. 18 zircons were selected from the non-magnetic, heavy fraction of the sample by hand picking under binocular microscope, mounted in epoxy resin, polished to flatness and to expose the interior of the zircons, cleaned with analytical grade ethanol, and coated with carbon. All of the grains were investigated to characterize any possible internal structure by cathodoluminescence (CL) imaging using a Philips XL 30 scanning electron microscope at the Swedish

Table 1
$^{40}Ar/^{39}Ar$ *Plateau and Inverse Isochron Ages for Basaltic Samples From the Macquarie Ridge Complex*[a]

General characteristics			Plateau characteristics						Isochron characteristics					Preferred age[b] (Ma ± 2σ)
Sample no.	Rock type	Material	Plateau age (Ma ± 2σ)	K/Ca	^{39}Ar (%)[d]	No. of steps	MSWD	p	Inv. Isochron age (Ma ± 2σ)	*n*	^{40}Ar/^{36}Ar intercept (± 2σ)	MSWD	*p*	
						Macquarie Island								
MQ17-06	Basalt	Groundmass	16.6 ± 2.3[c]	0.0036	85	13 of 21	0.48	0.93	16.8 ± 2.7	13	366 ± 39	0.56	0.86	-
MQ17-07	Besalt	Groundmass	**10.1 ± 2.2**	0.0025	95	19 of 21	0.89	0.59	8.6 ± 2.5	19	344 ± 93	0.88	0.59	**10.1 ± 2.2**
		Plagioclase	30.8 ± 2.8[c]	0.0018	100	22 of 22	0.95	0.52	31.2 ± 3.4	22	348 ± 45	0.66	0.87	-
MQ17-08	Besalt	Hornblende	**10.34 ± 0.30**[c]	0.0164	97	16 of 24	0.46	0.96	10.07 ± 0.78	16	309 ± 28	0.45	0.96	**10.34 ± 0.30**
MQ17-09	Glassy breccia	Glass	**10.00 ± 0.17**[c]	0.0151	99.9	20 of 21	0.16	1.00	10.00 ± 0.18	20	292.0 ± 1.1	0.19	1.00	**10.00 ± 0.17**
MQ17-10	Dolerite	Groundmass	62 ± 15	0.0010	64 (Mini-plateau)	7 of 21	0.79	0.58	73 ± 44	7	294 ± 33	0.93	0.46	-
MQ17-11	Gabbro	Groundmass	30 ± 10	0.0015	88	12 of 21	1.01	0.43	18 ± 10	12	320 ± 23	0.79	0.64	-
MQ17-12	Basalt	Groundmass	**10.2 ± 3.5**	0.0022	96	19 of 21	1.05	0.40			No isochron age			**10.2 ± 3.5**
		Sericite	6.3 ± 5.4	0.0016	100	18 of 18	0.44	0.98	6.1 ± 3.5	18	298.9 ± 2.5	0.49	0.95	-
MQ17-14	Basaltic dyke	Groundmass	16.1 ± 5.0	0.0039	80	14 of 21	0.3	0.99	12 ± 12	14	341 ± 183	0.31	0.99	-
						Seamount 3								
MRC-5	Basalt	Groundmass	7.50 ± 0.11	0.0694	54 (Mini-plateau)	7 of 21	0.73	0.62	7.54 ± 0.13	7	296.0 ± 1.1	0.93	0.46	-
MRC-6	Pillow glass	Glass	**1.59 ± 0.26**	0.0212	94	15 of 19	1.26	0.22	1.93 ± 0.57	15	292 ± 12	1.26	0.23	**1.59 ± 0.26**
MRC-7	Basalt	Groundmass	1.35 ± 0.71	0.0245	64 (Mini-plateau)	5 of 21	0.68	0.61	2.2 ± 1.4	5	295.9 ± 4.7	0.49	0.69	-
			3.65 ± 0.22	0.0512	63 (Mini-plateau)	7 of 21	1.28	0.26	3.5 ± 1.4	7	300 ± 15	1.54	0.17	-
MRC-8	Basalt	Groundmass	20.8 ± 1.4	0.0033	61 (Mini-plateau)	8 of 21	1.61	0.13	33.1 ± 8.1	8	268 ± 21	0.68	0.67	-
						Seamount 5								
MRC-2	Basalt	Groundmass	22.3 ± 1.8	0.0033	50 (Mini-plateau)	6 of 21	1.33	0.25	24.5 ± 3.6	6	282 ± 25	1.2	0.31	-
MRC-9	Basalt	Groundmass	3.63 ± 0.21	0.0513	64 (Mini-plateau)	5 of 21	1.11	0.35	4.32 ± 0.84	5	289 ± 11	0.63	0.60	-
		Groundmass	7.01 ± 0.25	0.0356	69.7 (Mini-plateau)	10 of 21	0.25	0.99	7.01 ± 0.30	10	295.1 ± 1.3	0.3	0.97	-
MRC-10	Basalt	Groundmass	20.4 ± 1.4	0.0051	68 (Mini-plateau)	8 of 21	1.59	0.13	22.6 ± 2.5	8	294.0 ± 4.7	1.15	0.33	-
MRC-11	Gabbro	Pyroxene	**10.90 ± 0.81**	0.0009	75	12 of 23	1.37	0.18	10.9 ± 1.2	12	299.01 ± 0.51	1.85	0.05	**10.90 ± 0.81**
						Seamount 6								
MRC-14	Basalt	Groundmass	**18.34 ± 0.53**	0.0059	100	21 of 21	1.01	0.44	17.6 ± 1.4	21	302.3 ± 6.3	1.01	0.44	**18.34 ± 0.53**
						Seamount 7								
MRC-16	Basalt	Plagioclase	**14.1 ± 1.2**[c]	0.0011	87	21 of 22	1.14	0.29	14.2 ± 2.1	21	293.3 ± 1.1	1.41	0.11	**14.1 ± 1.2**

Table 1
Continued

General characteristics			Plateau characteristics						Isochron characteristics					
Sample no.	Rock type	Material	Plateau age (Ma ± 2σ)	K/Ca	^{39}Ar (%)[d]	No. of steps	MSWD	p	Inv. Isochron age (Ma ± 2σ)	*n*	^{40}Ar/^{36}Ar intercept (± 2σ)	MSWD	*p*	Preferred age[b] (Ma ± 2σ)
						Seamount 8								
MRC-18	Dolerite	Hornblende	26.67 ± 0.31[c]	0.0447	74	9 of 25	11.01	0	26.27 ± 0.35	9	308.2 ± 6.1	6.05	0	-
		Sericite	**16.1 ± 1.8**	0.027	79	14 of 16	0.91	0.54	16.6 ± 3.1	14	298.6 ± 7.0	1.16	0.30	**16.1 ± 1.8**
		Sericite	**18.0 ± 1.1**	0.026	93	12 of 14	0.68	0.76	17.4 ± 2.8	12	300.5 ± 7.7	0.78	0.65	**18.0 ± 1.1**
						Seamount 9								
MRC-21	Basaltic breccia	Groundmass	18.19 ± 0.28	0.0126	60 (Mini-plateau)	7 of 21	1.21	0.30	18.13 ± 0.61	7	299.3 ± 7.3	1.44	0.21	-
						Seamount 10								
MRC-4	Gabbro	Pyroxene	**25.90 ± 0.23**[c]	0.0123	92	12 of 24	0.6	0.83	25.91 ± 0.50	12	293.5 ± 0.7	0.84	0.59	**25.90 ± 0.23**

[a]Detailed analytical data, including 26 analyses that failed to produce plateau or mini-plateau, are provided in Table S4. Ages in bold are statistically robust ages. [b]Errors include all sources of uncertainties calculated following the error propagation approach of Renne et al. (2010) based on Monte Carlo simulations and appropriate R-values. [c]Measured ^{40}Ar/^{36}Ar intercept ratio was used to calculate the plateau age. [d]Value applies for both the plateau and inverse isochron calculations.

Museum of Natural History (Stockholm, Sweden). The accelerating voltage was set to 15 kV and the working distance was 20.6 mm. The U–Pb and oxygen isotope measurements were performed using a CAMECA IMS 1280 ion microprobe at the NordSIMS facility of the Swedish Museum of Natural History. The data were reduced using an in-house Excel add-in. Weighted averages and concordia plots were made using the Excel add-in, Isoplot (Ludwig, 2008).

4.2.1. Oxygen Isotopes

Oxygen isotopes were measured using a 10 kV Cs^+ primary beam with a Gaussian profile at a working intensity of ∼ 3 nA. The instrument was operated with a 40 eV energy window, 3,000 μm field aperture, 150 μm entrance slit and 400 μm contrast aperture. Dynamic Transfer Optical System (DTOS) mode was activated and the transfer magnification was set to × 90. The resulting field of view was ∼33 μm. The spot size was ∼10 μm. The analyses were performed with the mass resolution ($M/\Delta M$) set to 2,460. The samples were sputtered before analysis for 50 s using a raster size of 20 × 20 μm. ^{16}O and ^{18}O isotopes were measured using Faraday cups in multi-collection mode. Each measurement consisted of 12 cycles and, for each cycle, the integration time was 4 s and the wait time was 0.8 s for the ^{16}O and ^{18}O isotopes. Corrections for instrumental mass fractionation were performed using a standard-sample bracketing external normalization method in which standards were analyzed at regular intervals after each block of six unknowns (five samples and one secondary standard) in fully automated chain sequences; this routine also enabled monitoring of, and correction for, any minor drift.

M257 zircon was initially used as primary standard (accepted values: $\delta^{18}O = 13.93 \pm 0.11‰$ relative to Vienna Standard Mean Ocean Water; Nasdala et al., 2008) and Penglai zircon was used as a secondary standard (accepted values: $\delta^{18}O = 5.31 \pm 0.20\%$, 2σ; Li et al., 2010). Two analyses of M257 and one of Penglai were made after every five analyses of the unknowns. The measured values of the Penglai standard yielded $\delta^{18}O = 5.03 \pm 0.12\%$ ($n = 7$; 2σ), which is marginally lower than the accepted values. To investigate this discrepancy between the measured values and accepted values of the Penglai standard, we conducted a second analytical session during which the same M257 and Penglai grains were re-mounted along with the 91,500 zircon standard (accepted values: $\delta^{18}O = 9.86 \pm 0.22\%$, 2σ; Wiedenbeck et al., 2004) and re-analyzed after polishing of the mount to remove the original SIMS pits. Both standards were reduced against 91,500 in this second session. The Penglai standard yielded $\delta^{18}O = 5.31 \pm 0.06\%$ (2σ, $n = 12$), which is in agreement with the accepted values, while M257 yielded $\delta^{18}O = 14.13 \pm 0.06\%$ (2σ), which is slightly higher than the accepted values ($\Delta = 0.03\%$). Therefore, we suspect an heterogeneity among the M257 grains in terms of oxygen isotopes. As a consequence, the unknowns were reprocessed using Penglai as a primary standard. The secondary standard from the first session yielded an average value of $\delta^{18}O = 14.10 \pm 0.07\%$ (2σ, $n = 14$), which is marginally higher than the accepted value ($\Delta = 0.17\%$).

4.2.2. U–Pb Geochronology

For the U–Pb measurements, the targets were analyzed using a −13 kV $^{16}O^{2-}$ primary beam (10 kV secondary beam) with a Gaussian profile at a working intensity of 10 nA. The instrument was operated with a 45 eV energy window, 3,001 μm field aperture, 75 μm entrance slit and 400 μm contrast aperture. Transfer magnification was set to ×160, and the resulting field of view was ∼18 μm. The spot size was ∼15 μm. The analyses were performed at a mass resolution (M/ΔM) of 5,394. The samples were sputtered before analysis for 60 s using a raster size of 25 × 25 μm. Analyses were made using O_2 flooding at a pressure of 0.016×10^{-3} mbar. The ^{204}Pb, ^{206}Pb, ^{207}Pb and ^{208}Pb isotopes were measured in mono-collection using the axial ion counting electron multiplier (peak jumping mode). Each measurement consisted of 10 cycles. For each cycle, integration time was 0.48 s for $^{90}Zr^{16}O_2$; 2.96 s for mass 200.5; 4.96 s for ^{204}Pb and ^{207}Pb; 3.2 s for ^{206}Pb; 1.6 s for ^{208}Pb and $^{238}U^{16}O$; 0.24 s for $^{177}Hf^{16}O_2$; 0.96 s for ^{232}Th and $^{232}Th^{16}O$; 2 s for ^{238} and $^{238}U^{16}O_2$. The corresponding wait time was set at 2 s for $^{90}Zr^{16}O_2$, 0.8 s for 200.5, ^{204}Pb ^{206}Pb, ^{207}Pb, ^{208}Pb and $^{177}Hf^{16}O_2$; 1.12 s for ^{232}Th; 0.88 s for ^{238}U, 0.96s for $^{232}Th^{16}O$, 0.88 s for $^{238}U^{16}O_2$ and 1.04 s for $^{238}U^{16}O_2$. Measured Pb/U ratios were calibrated using an empirical correlation between Pb^+/U^+ and $UO_2{}^+/U^+$ ratios, normalized to the values obtained from analyses of M257 zircon standard ($^{206}Pb/^{238}U$ age: 561.3 ± 0.3 Ma, 95% confidence; Nasdala et al., 2008). Penglai zircon ($^{206}Pb/^{238}U$ age: 4.4 ± 0.1 Ma, 95% confidence; Li et al., 2010) was also analyzed as a secondary standard. The ^{204}Pb counts were low (Table S3), so the unknowns were not corrected systematically for common Pb (Table S3). When a correction was applied, the isotopes ^{204}Pb or ^{208}Pb (when the ^{204}Pb correction yielded an overcorrection of the isotopic ratios than a reverse discordance) were used as proxies for common Pb, and ratios of the average composition of modern terrestrial Pb (Stacey & Kramers, 1975) were used. The errors were calculated by propagating the analytical uncertainties. Ellipses are shown as 2σ level on the concordia diagrams (Figure 5). Seven analyses of Penglai zircon yielded an average age of 4.41 ± 0.21 Ma (2σ, MSWD = 1.6, $p = 0.13$; Table S3), which is in agreement with the accepted values of Li et al. (2010).

5. Results

The $^{40}Ar/^{39}Ar$ geochronology results are summarized in Table 1 and a representative selection of acceptable age spectra obtained for each of the basaltic samples on plagioclase, pyroxene, glass, sericite, and groundmass is shown in Figure 3. The remaining age spectra and detailed analytical results are provided in Figure S1 and Table S1, respectively. The results of zircon U–Pb geochronology and oxygen isotope analysis are presented in Figures 4 and 5 and Tables S2–S3. The errors on $^{40}Ar/^{39}Ar$ and U–Pb ages include all sources of uncertainties and are reported at the 2σ level.

5.1. $^{40}Ar/^{39}Ar$ Ages of MRC Seamounts

5.1.1. Seamount 3

Ten analyses were conducted for Seamount 3 (Table 1; Figures 3 and S1). One glass sample yielded a 94% (i.e., including 94% of the total ^{39}Ar released) plateau age of **1.59 ± 0.26 Ma** ($p = 0.22$; MRC-6, Figure 3). The K/Ca ratio is homogeneous with an average value of 0.0212. Other groundmass and plagioclase samples did not produce robust plateau ages, which is attributed to alteration, and/or excess Ar, and/or the low K content in plagioclase of MORBs and the young ages which hindered the ingrowth of enough amount of radiogenic Ar to be accurately measured (Figure S1).

5.1.2. Seamount 5

Eight analyses were conducted (Table 1). A pyroxene sample yielded a plateau age of **10.90 ± 0.81 Ma** ($p = 0.18$) with 75% of the total ^{39}Ar released (MRC-11, Figure 3). The K/Ca spectrum shows large uncertainties on K/Ca in the first few steps, which is probably associated with degassing of the low-Ca pyroxene pigeonite, and ultralow K/Ca ratios at the end of the spectrum, which is attributed to Ar released from high-Ca pyroxene lamellae exsolutions. These features are characteristic of pyroxene Ar degassing (Ware & Jourdan, 2018). The K/Ca ratios of steps forming the age plateau range from 0.0225 to 0.0005 (Figure 3). The other seven analyses either failed to yield plateaus (MRC-9 plagioclase) or yielded groundmass mini-plateaus that are probably meaningless (Table 1, Figure S1).

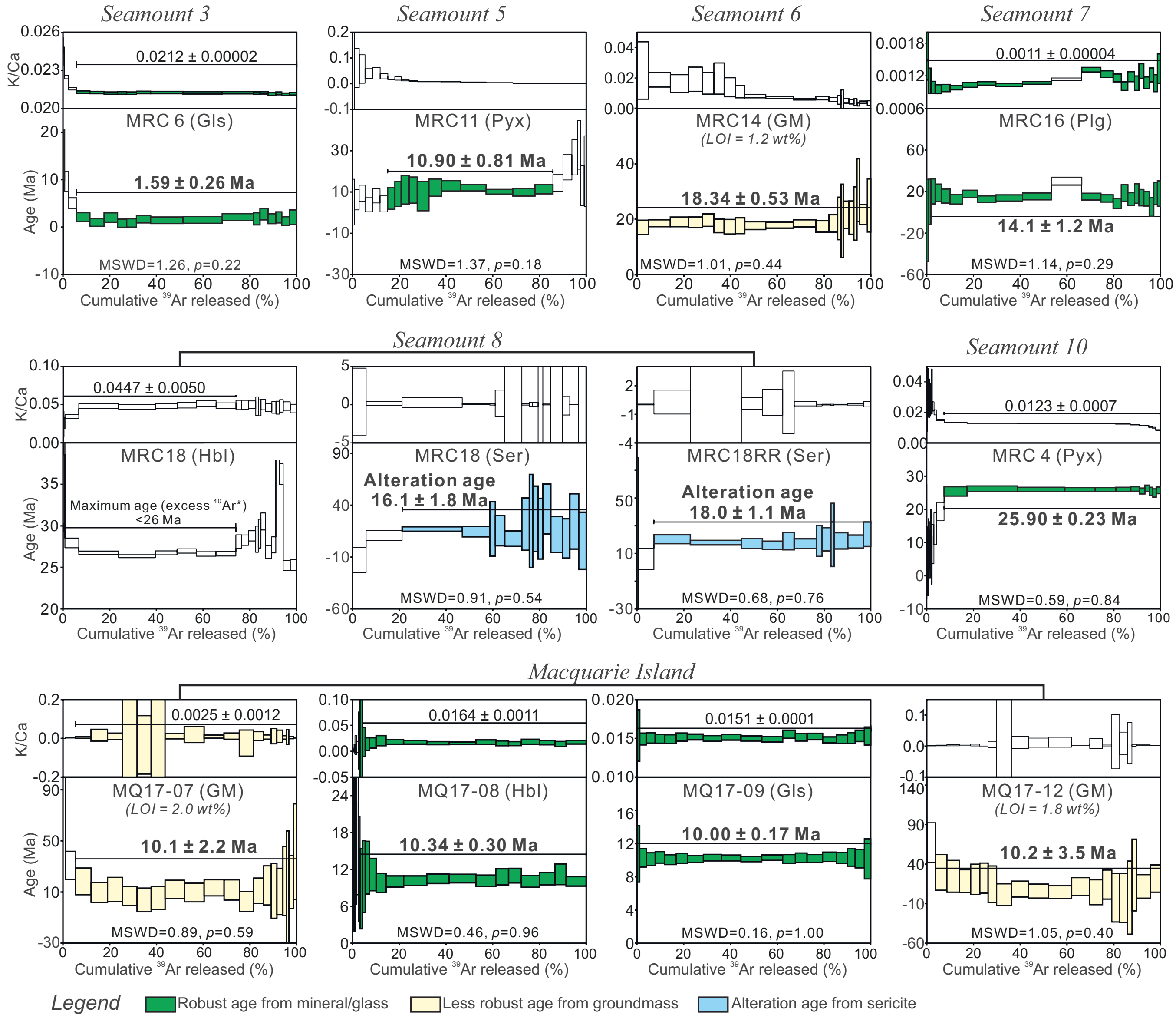

Figure 3. Selected ^{40}Ar/^{39}Ar spectra versus cumulative ^{39}Ar released. The age uncertainties (2σ) include all sources of error. Gls, glass, GM, groundmass, Hbl, hornblende, LOI, loss on ignition, Plg, plagioclase, Pyx, pyroxene, Ser, sericite.

5.1.3. Seamount 6

Two plagioclase samples failed to yield plateau ages, probably due to the presence of excess Ar, as indicated by the saddle-shaped age spectra (Figure S1). A groundmass plateau including 100% of the released ^{39}Ar indicates that the age of this seamount is probably **18.34 ± 0.53 Ma** ($p = 0.44$; MRC-14, Figure 3). The other groundmass sample (MRC-12) and a pyroxene (MRC-3) did not yield plateau ages.

5.1.4. Seamount 7

Three samples were analyzed (Table 1). The age of Seamount 7 is constrained to **14.1 ± 1.2 Ma** ($p = 0.29$) by a plagioclase plateau including 87% of the total ^{39}Ar released, and an associated K/Ca ratio of 0.0011 (Figure 3). One step in the age spectra yielded an apparent age of 30.0 ± 3.7 Ma, which is older than the apparent ages of the other steps, attributed to degassing of a melt inclusion that contains excess Ar. Therefore, this step is not in-

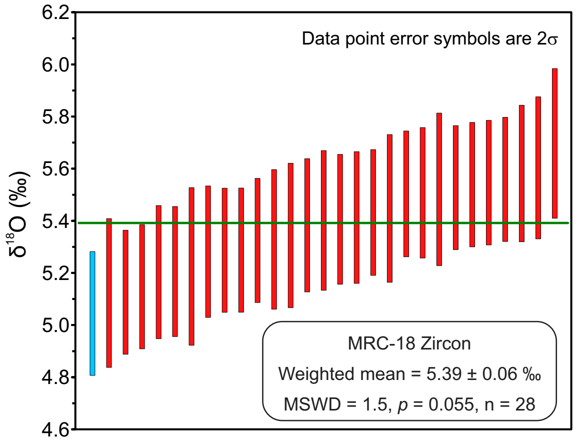

Figure 4. Oxygen isotope data of MRC-18 zircons from Seamount 9. Data that are included and not included in calculating the weighted mean value are colored in red and blue, respectively.

cluded in the calculation of the plateau age (Figure 3). The plagioclase sample MRC-15 and groundmass sample MRC-16 failed to yield plateau ages.

5.1.5. Seamount 8

Four aliquots from a single sample from Seamount 8 were analyzed. The saddle-shaped age spectrum produced by a hornblende sample indicates the existence of excess radiogenic ^{40}Ar and that the sample is younger than 26 Ma (Figure 3). The sericite plateau ages of 16.1 ± 1.8 Ma ($p = 0.54$) and 18.0 ± 1.1 Ma ($p = 0.76$) from the same sample are concordant and yield a weighted mean age of **17.48 ± 0.94 Ma**, which constrains the age of hydrothermal alteration of this sample (Olierook et al., 2017; Verati & Jourdan, 2014). Therefore, the ^{40}Ar/^{39}Ar data indicate that the eruption age of sample MRC-18 from Seamount 8 is 26–18 Ma.

5.1.6. Seamount 9

A groundmass sample yielded a 60% mini-plateau age of 18.19 ± 0.28 Ma ($p = 0.30$; MRC-21; Table 1, Figure S1), which is not considered robust according to the criteria established above and is not used in the following discussion. The groundmass sample MRC-21 and plagioclase sample MRC-22 failed to yield age plateaus, probably due to alteration and/or the presence of excess Ar (Figure S1).

5.1.7. Seamount 10

The age of Seamount 10 is well constrained by a ^{40}Ar/^{39}Ar plateau at **25.90 ± 0.23 Ma** ($p = 0.83$; Figure 3) from a pyroxene sample (cf. Energy Dispersive X-ray analysis in the Supporting Information) with 83% of the total ^{39}Ar released. The K/Ca ratios show a different pattern to that of pyroxene sample MRC-11, possibly because the pyroxene sample is more enriched in K and/or less enriched in Ca compared to typical pyroxene, and/or because of an absence of pigeonite, then augite, degassing that is typical of pyroxene samples (Ware & Jourdan, 2018).

5.2. U-Pb Ages and Oxygen Isotopic Compositions of Zircon from Seamount 8

Eighteen zircon crystals were analyzed from the dolerite sample MRC-18**.** The investigated grains have subhedral morphologies, average grain lengths of ∼100 μm and length-to-width ratios of ∼1:1 to 2:1. Internally, CL imaging reveals that most grains have oscillatory zoning and/or sector zoning (Figure S3) that are characteristic of igneous zircon. With the exception of one crystal (Zircon 15; Figure S3), the grains do not show inherited cores. The 29 oxygen isotope analyses yielded δ^{18}O values of 5.05 ± 0.24%–5.70 ± 0.28% (2σ; Table S2). Except one analysis (Zrc4-#6), the data overlap within uncertainty, including those of the core of Zircon 15. The weighted-mean δ^{18}O is 5.39 ± 0.05% (2σ, $n = 28$, MSWD = 1.45; $p = 0.055$; Figure 4). This value is similar to those of zircon grains in equilibrium with the mantle (5.3 ± 0.3%, 1σ; Valley et al., 1998) and those of zircon grains from ophiolites (3.9%–5.6%; Grimes et al., 2013).

Nineteen U–Pb analyses were performed on 17 of the 18 grains that were also analyzed for oxygen isotopes. Two analyses were performed on grains 4 and 17 and, in both cases, the ^{207}Pb-corrected ^{206}Pb/^{238}U ages are identical within error (Table S3). All data are concordant, and cluster on concordia at ∼26 Ma, with a slight spread toward lower ^{206}Pb/^{238}U and ^{207}Pb/^{235}U (Figure 5). For each analysis, a ^{207}Pb-corrected ^{206}Pb/^{238}U age can be calculated that assumes ^{206}Pb/^{238}U-^{207}Pb/^{206}Pb age concordance, based on the concordant data, and the single igneous zircon population indicated by the oxygen data. Any discordance is attributed to small amounts of common Pb. From these ^{207}Pb-corrected ^{206}Pb/^{238}U ages, a weighted-mean age of 25.82 ± 0.18 Ma (2σ; 2 data points rejected; $n = 17$, MSWD = 1.4, $p = 0.13$; Figure 5) was calculated. This age is within uncertainty of the lower intercept of 26.56 ± 0.76 Ma (2σ vs. 95% confidence), so we consider the weighted-mean age of **25.82 ± 0.18 Ma** to represent the timing of formation of sample MRC-18. This age is consistent with ages derived from hornblende (< 26 Ma) and sericite (> 18 Ma) ^{40}Ar/^{39}Ar geochronology (Figure 3), which indicates that hydrothermal alteration event was not syn-emplacement, but reflects late hydrothermal activity.

5.3. ^{40}Ar/^{39}Ar Ages of Macquarie Island

A total of 20 analyses were conducted on samples from Macquarie Island (Table 1). On the northern tip of the island, a groundmass sample (MQ17-14) yielded an apparent plateau age of 16.1 ± 5.0 Ma ($p = 0.99$; Table 1, Figure S1). However, the plateau contains age steps with very large uncertainties (2σ uncertainties ranging from 74%–406%; Table S1), and might represent a fortuitous plateau, with complexity masked by the large error bars (cf. Jourdan et al., 2012; Kennedy et al., 2019) that does not reflect the true age of the sample. The groundmass sample MQ17-15 is similar to MQ17-14, and also produced large uncertainties for individual steps that did not form an age plateau (Figure S1).

Two groundmass samples, MQ17-06 and MQ17-07, from the central northern portion of the island yielded plateau ages of 16.6 ± 2.3 Ma ($p = 0.93$; MQ17-06) and **10.1 ± 2.2 Ma** ($p = 0.59$; MQ17-07). However, alteration minerals (e.g., chlorite, zeolite, and sericite; Figures 2a and 2b) are common in the groundmass, and the LOI of sample MQ17-06 (LOI = 3.2 wt.%) is higher than that of sample MQ17-07 (Figure S2; LOI = 2.0 wt%; Jiang et al., 2020), so the plateau age of sample MQ17-06 is likely to be older than its true crystallization age, based on the probable loss of K_2O from the glass component. Groundmass sample MQ17-10 yielded a 64% mini-plateau age with a large uncertainty (Table 1, Figure S1). Plagioclase from sample MQ17-07 and groundmass from sample MQ17-11 yielded spuriously old apparent plateau ages of ~30 Ma (Table 1, Figure S1). The age steps of the plateaus show large uncertainties, similar to that of the groundmass sample MQ17-14, and may only represent fortuitous plateaus. Furthermore, a slight saddle-shape pattern hints at the presence of excess Ar. Therefore, these data are not considered further.

A hornblende sample from the central southern portion of the island, yielded a plateau age of **10.34 ± 0.30 Ma** ($p = 0.96$; MQ17-08) with 97% ^{39}Ar released and an average K/Ca of 0.0164, and a glass sample produced a plateau age of **10.00 ± 0.17 Ma** ($p = 1.00$; MQ17-09) with 99.9% of the total ^{39}Ar released and an average K/Ca of 0.0151 (Table 1, Figure 3).

A fresh groundmass sample from the southern end of the island yielded a plateau age of **10.2 ± 3.5 Ma** ($p = 0.40$; MQ17-12, Figure 3) with 96% ^{39}Ar released.

6. Discussion

6.1. Timing of Volcanism at the Macquarie Ridge Complex

6.1.1. Macquarie Ridge Complex Seamounts

^{40}Ar/^{39}Ar plateau ages indicate that basalts from Seamount 10 on the southern Hjort segment of the MRC were erupted at 25.90 ± 0.23 Ma (Figure 1). On the Macquarie segment, zircon U-Pb and ^{40}Ar/^{39}Ar plateau ages indicate that basalts from Seamount 8 and Seamount 7 formed at 25.82 ± 0.18 Ma and 14.1 ± 1.2 Ma, respectively. The basalts exposed on Macquarie Island on the Macquarie segment formed at ~10 Ma according to the four statistically robust ^{40}Ar/^{39}Ar plateau ages. On the McDougall segment, basalts sampled at Seamount 6 were erupted at 18.34 ± 0.53 Ma and at 10.90 ± 0.81 Ma for Seamount 5. One sample recovered from Seamount 3 on the northern Puysegur segment was erupted at 1.59 ± 0.26 Ma (Figure 1).

6.1.2. Macquarie Island

Two statistically robust hornblende (MQ17-08) and glass (MQ17-09) ^{40}Ar/^{39}Ar plateau ages of 10.34 ± 0.30 Ma and 10.00 ± 0.17 Ma, supported by two groundmass (MQ17-07, −12) ^{40}Ar/^{39}Ar plateau ages of 10.1 ± 2.2 Ma and 10.2 ± 3.5 Ma are all indistinguishable within error ($n = 4$; $p = 0.27$) and indicate that basalts on Macquarie Island formed at ~10 Ma (Figures 1 and 3). Two ^{40}Ar/^{39}Ar plateau ages of 11–9 Ma from two samples showing obvious evidence of alteration were published previously (Duncan & Varne, 1988), but their accuracy within the reported uncertainties cannot be verified because of the lack of (i) reported/re-calculable statistical parameters, such as MSWD and/or p (probability of fit) to test for data

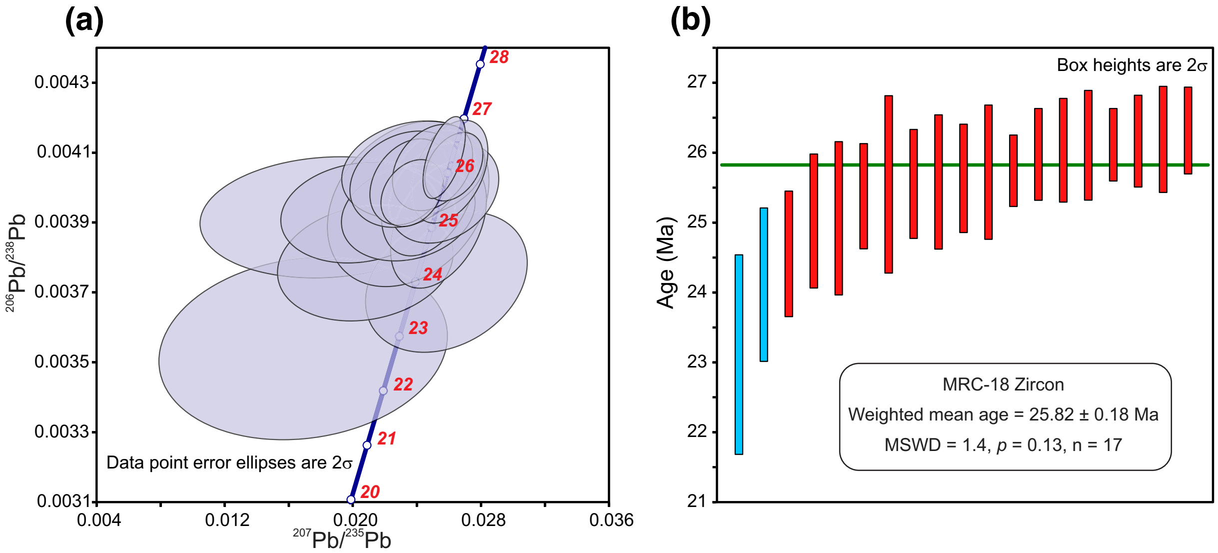

Figure 5. (a) Concordia and (b) ^{207}Pb-corrected ^{206}Pb/^{238}U weighted mean age plots for zircon of sample MRC18 from Seamount 9. The age uncertainty (2σ) includes all sources of error. Data that are included and not included in calculating the weighted mean value are colored in red and blue, respectively.

internal concordance as well as closed system behavior (e.g., absence of alteration; Baksi, 2007; Jourdan et al., 2012); (ii) isochron data, to test whether the trapped ^{40}Ar/^{36}Ar ratio is atmospheric (i.e., 298.56; Lee et al., 2006) and if not, to calculate the age using the correct value (e.g., Oostingh et al., 2017); and (iii) neutron flux monitor standard information to which the ages were calculated relative to. However, these ages are consistent with crystallization at ∼10 Ma and with the ages presented in this study.

6.2. Magmatic and Tectonic Evolution of the Macquarie Ridge Complex

The geodynamic processes and timing of seafloor spreading cessation on the proto-Macquarie mid-ocean ridge remain elusive. The youngest magnetic anomaly identified adjacent to the central McDougall and Macquarie segments is Chron C7 (∼24 Ma; Keller, 2004), and on the northern (Puysegur) and southern (Hjort) segments, it is Chron C11 (∼30 Ma; Keller, 2004; Massell et al., 2000). However, closer to the ridge, the fracture zones became curved and apparent distances between fracture zones decreased (Figure 6i; Keller, 2004; Massell et al., 2000) as a result of right lateral strike-slip motions along the MRC in the last ∼30 Ma (Lamarche et al., 1997). These closely spaced fracture zone patterns have hampered the identification of magnetic anomalies close to the MRC and impeded accurate plate reconstructions of the late stages of seafloor spreading. Previously, plate reconstructions of the Macquarie Basin were only available from ∼40-30 Ma (Keller, 2004) and it was postulated that spreading-related magmatism ceased at ∼6 Ma (Mosher & Symons, 2008; Wertz, 2003). Our new ^{40}Ar/^{39}Ar and zircon U–Pb ages ranging from 25.90 ± 0.23 Ma to 1.59 ± 0.26 Ma, define systematic variations in age from the south to the north of the MRC, and provide new constraints on the magmatic and tectonic evolution of the proto-Macquarie spreading center during the cessation of spreading. These results allow us to model the plate tectonic configuration of the Macquarie Basin from the initial stages of spreading (just before ∼40 Ma) to present day.

We have used GPlates software to reconstruct the paleogeographic evolution of the Macquarie Basin since 42 Ma. In this reconstruction, the starting positions of the Australian and Pacific Plates (Figure 6a) and the rotation poles of these plates are from Seton et al. (2012). The fracture zones and magnetic anomalies of the Macquarie Basin (Figure 6i) are those of Massell et al. (2000) and Keller (2004).

Basalts on the MRC were formed during the final stages of volcanism of the spreading center (Mosher & Symons, 2008; Wertz, 2003). Indeed, basalts produced by the spreading center at earlier stages should have moved away from the ridge as spreading continued. However, it is possible that magmatic activity

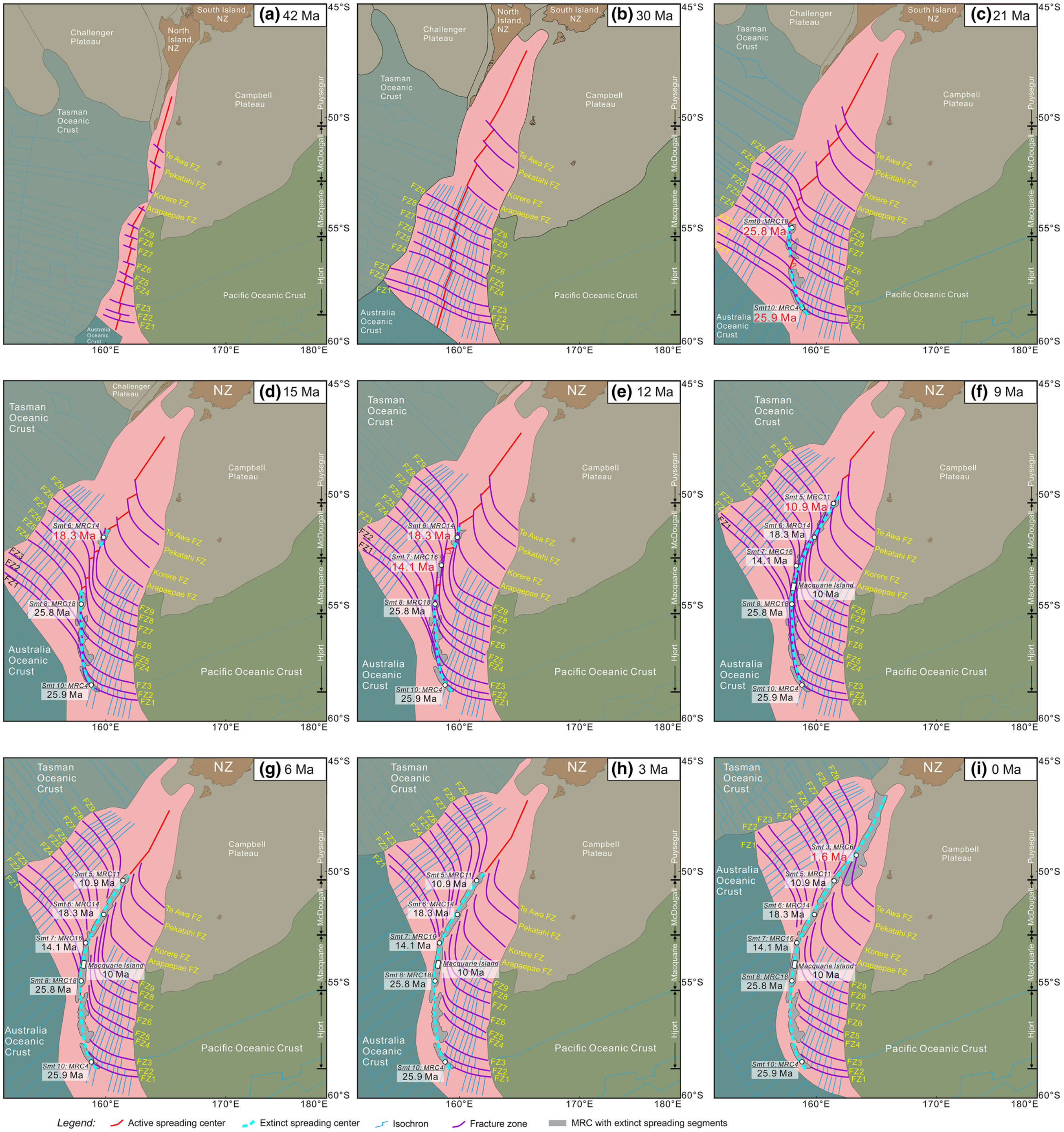

Figure 6. Plate reconstructions of the Macquarie Basin at (a) 42 Ma, (b) 30 Ma, (c) 21 Ma, (d) 15 Ma, (e) 12 Ma, (f) 9 Ma, (g) 6 Ma, (h) 3 Ma, and (i) 0 Ma, in a fixed Pacific reference frame. The fracture zones and magnetic anomalies of present day (i) are from Keller (2004) and Massell et al. (2000). The starting plate positions (a) and rotation poles are from Seton et al. (2012).

on abandoned spreading ridges continues for a few million years after the cessation of seafloor spreading. For instance, ^{40}Ar/^{39}Ar data from the dying Phoenix Ridge show that magmatism continued for over 2 Ma after seafloor spreading ceased (Haase et al., 2011b). In another example, the Mathematicians Ridge stopped spreading at ~3.5 Ma when spreading transferred to the East Pacific Rise, but eruptions continued episodically until present-day on Socorro Island (Bohrson et al., 1996). However, magmatic activity following cessation of ridge-spreading appears to be relatively short-lived in the cases mentioned above. For the MRC, the seamount samples were dredged on the top of the ridge crest (Conway et al., 2012) and are likely to be the youngest volcanic products prior to spreading cessation. Samples from Macquarie Island all yielded $^{40}Ar/^{39}Ar$ ages of ∼10 Ma without obvious variation. Therefore, we consider the ages obtained from each MRC seamount and Macquarie Island as the timing of cessation of seafloor spreading at that part of the ridge with a reasonable accuracy, although more samples and age data from each MRC seamount and Macquarie Island are still needed to assess the durations and episodicities (if any) of magmatism. We note that the strike-slip motions along the MRC between the Australian and Pacific Plates means that the oceanic crust might have been displaced from the location of its eruption. However, our reconstruction results show that most of the dextral motions between the two plates were accommodated by the re-orientation of spreading directions (Figure 6), and most of the faults observed along the ridge are dip-slip faults, and strike-slip faults that developed on the flanks of the ridge (Conway et al., 2012), without obvious evidence that the ridge crest where the samples were collected was displaced significantly.

The $^{40}Ar/^{39}Ar$ plateau age of 25.90 ± 0.23 Ma (Figure 3) obtained from Seamount 10 and U-Pb age of 25.82 ± 0.18 Ma (Figure 5) from Seamount 8 indicate that seafloor spreading ceased by ∼26 Ma on the Hjort and southern Macquarie segments (Figure 6c). This was probably caused by the right lateral strike-slip motions between the Australian and Pacific Plates, which caused the arcuate bends in the fracture zones, decreases in fracture zone spacing, and gradual shortening and eventual disappearance of spreading segments that sustained active magmatism (Mosher & Symons, 2008). We infer that short active spreading segments persisted until ∼25.8 Ma on the central and northern Hjort segments (Figure 4c), based on the relatively large distance between fracture zones FZ3 and FZ4.

The ages of basalts from Macquarie Island are constrained at ∼10 Ma by a hornblende (MQ17-08), a glass (MQ17-09) and two groundmass (MQ17-07, −12) samples, although more data from various eruptive units across the island would be needed to assess the true duration of basaltic eruptions on the island. Based on the dating results, we infer that seafloor spreading ceased by ∼10 Ma on the central Macquarie segment where Macquarie Island is located. The cessation of seafloor spreading on the northern Macquarie segment is recorded by a plagioclase $^{40}Ar/^{39}Ar$ plateau age of 14.1 ± 1.2 Ma from Seamount 7 (Figure 6e). We note that although Seamount 8, Macquarie Island, and Seamount 7 are currently all seated on the Macquarie segment (Figure 1a), which is one of the four segments that are defined based on the discontinuities and changes in orientation of the current Macquarie Ridge (e.g., Massell et al., 2000), they were produced by different active spreading segments which were disappeared at different times. Our new age data show that seafloor spreading ceased on the Hjort and Macquarie segments in the southern half of the MRC by ∼10 Ma (Figure 6c–6e).

The northern half of the MRC yields a groundmass $^{40}Ar/^{39}Ar$ plateau age of 18.34 ± 0.53 Ma from Seamount 6, indicating that spreading-related magmatism on the central portion of the McDougall segment might have ceased before that on the central and northern parts of the Macquarie segment (Figures 6d and 6e), although it would be useful to corroborate the groundmass age from Seamount 6 with a more robust mineral $^{40}Ar/^{39}Ar$ plateau age. Moreover, the timing of the cessation of spreading on the southern portion of the McDougall segment (south of Seamount 6; Figure 6e) remains unclear. A pyroxene $^{40}Ar/^{39}Ar$ plateau age of 10.90 ± 0.81 Ma from Seamount 5 on the northern McDougall segment indicates that seafloor spreading on the McDougall segment ceased by ∼11 Ma.

Only one $^{40}Ar/^{39}Ar$ plateau age, of 1.59 ± 0.26 Ma from a basaltic glass sample, is available for the Puysegur segment, which suggests that volcanism might have persisted until ∼1.6 Ma (Figure 6i). Constraints on the magmatic and tectonic evolution of the Puysegur segment remain challenging, because only four fracture zones have been identified on Pacific side of the MRC, to the north of fracture zone FZ9 (Figure 6; Keller, 2004; Massell et al., 2000). So more data are needed to explore whether the new age we obtained indicates that spreading-related volcanism persisted until ∼1.6 Ma or it represents the age of a post-spreading volcanic activity.

In summary, cessation of spreading-related magmatism on the MRC was diachronous. There is some indication that cessation of seafloor spreading propagated from south to north along the proto-Macquarie mid-ocean ridge given the general age progression along the MRC.

6.3. Chemical Characteristics the MRC MORBs in a Temporal Context

Mid-ocean ridge basalts produced by the proto-Macquarie mid-ocean ridge have highly variable chemical and isotopic characteristics. For example, major and trace element data indicate that the composition of the MRC basalts define a continuum from depleted MORB to a highly enriched MORB end-member (Conway et al., 2012; Jiang et al., 2020; Kamenetsky et al., 2000). Strontium, Nd and Pb isotopic data show that the composition of the MRC basalts extends from depleted MORB toward a HIMU-like mantle component (Jiang et al., 2020; Kamenetsky et al., 2000; Kamenetsky & Maas, 2002). Based on our new geochronology data and published geochemical and isotopic data, the temporal variation of the geochemical heterogeneity of the MRC basalts can be established.

Figure 7 shows the $^{206}Pb/^{204}Pb$, $^{207}Pb/^{204}Pb$, $^{208}Pb/^{204}Pb$, $^{143}Nd/^{144}Nd$, and La/Sm ratios versus ages for basalts from the MRC seamounts and Macquarie Island. We obtained only one robust age for each seamount and four ages for Macquarie Island (Table 1). Given that the four ages for Macquarie Island overlap with each other, the age difference for different samples from the same seamount should not be obviously different, although more robust age data are needed to confirm this. Therefore, the same age is used for different samples for each of the seamount for the plots (Figure 7). The isotopic ratios and ages show no clear temporal covariation ($R^2 = 0.11$, 0.13, 0.12, and 0.01, respectively; Figure 7). The isotopic ratios show large variations for each seamount/island, especially for Macquarie Island where more analyses and age data are available (Figure 7). Unfortunately, only one robust age is available for each of the MRC seamounts (Table 1), and for Macquarie Island, the age difference (if any) is not able to be distinguished due to the uncertainties of the $^{40}Ar/^{39}Ar$ age data, so currently it is not possible to establish trends in intra-seamount isotopic variations with time.

The geochemical data of the MRC basalts do, however, show covariations between isotopic ratios and La/Sm for the MRC basalts (Figure 8), but no covariation between isotopic ratios and Dy/Yb (Figure S4; Jiang et al., 2020). This indicates that the isotopic ratio variations of the MRC basalts are controlled by difference in partial melting degrees, rather than mixing between enriched and depleted mantle components. The covariations suggest that basalts produced at lower degrees of partial melting have more enriched isotopic compositions (Figure 8). With the cessation of seafloor spreading and reduction of spreading-related magma generation, the degree of partial melting at a dying mid-ocean ridge would decrease (e.g., Dick, 1989). At low degrees of partial melting, the enriched and more fusible components in the upper mantle are preferentially melted. Therefore, isotopically enriched basalts from each seamount/island should be formed by lower degrees of partial melting relative to basalts with isotopically more depleted compositions, and the more enriched basalts might have formed during later stages of magma generation, as seafloor spreading slowed. This trend of progressive decrease in degrees of partial melting and corresponding increase in enrichment is similar to the mantle source evolution at other dying mid-ocean ridges, such as the fossil Phoenix Ridge (Choe et al., 2007; Haase et al., 2011b) and the fossil spreading ridges off Baja California Sur (Castillo et al., 2010; Tian et al., 2011). The timing of shutdown of seafloor spreading and cessation of spreading-related magmatism varied for different segments over the MRC (Figure 6), so the chemical evolution of the MRC seamounts and Macquarie Island would have been spatially and temporally decoupled, which produced the chemical heterogeneity of the seamounts and Macquarie Island, and the lack of covariation between the ages and isotopic compositions of the MRC basalts (Figure 7).

6.4. Implications for Upper Mantle Heterogeneity

The presence of isotopically enriched basalts at every MRC seamounts and Macquarie Island indicates that an enriched mantle component occurs everywhere along the entire Macquarie Ridge (Figure 7). This indicates the mantle source for MORB from the MRC is heterogeneous on a small scale with low-volume patches of enriched components distributed within the upper asthenospheric mantle and homogeneously mixed on a plate boundary scale. Similar to the MRC MORB, heterogeneous and/or enriched MORBs have also been documented from other dying mid-ocean ridges, such as the Phoenix Ridge off the Antarctic Peninsula (Choi et al., 2008; Haase et al., 2011b) and the Galapagos Rise fossil ridge (Haase et al., 2011a), and ultraslow spreading ridges, such as the Gakkel Ridge in the Arctic Ocean (Mühe et al., 1997) and the Southwest Indian Ridge (9–25°E; Standish et al., 2008). A common feature of these mid-ocean ridges is that the overall

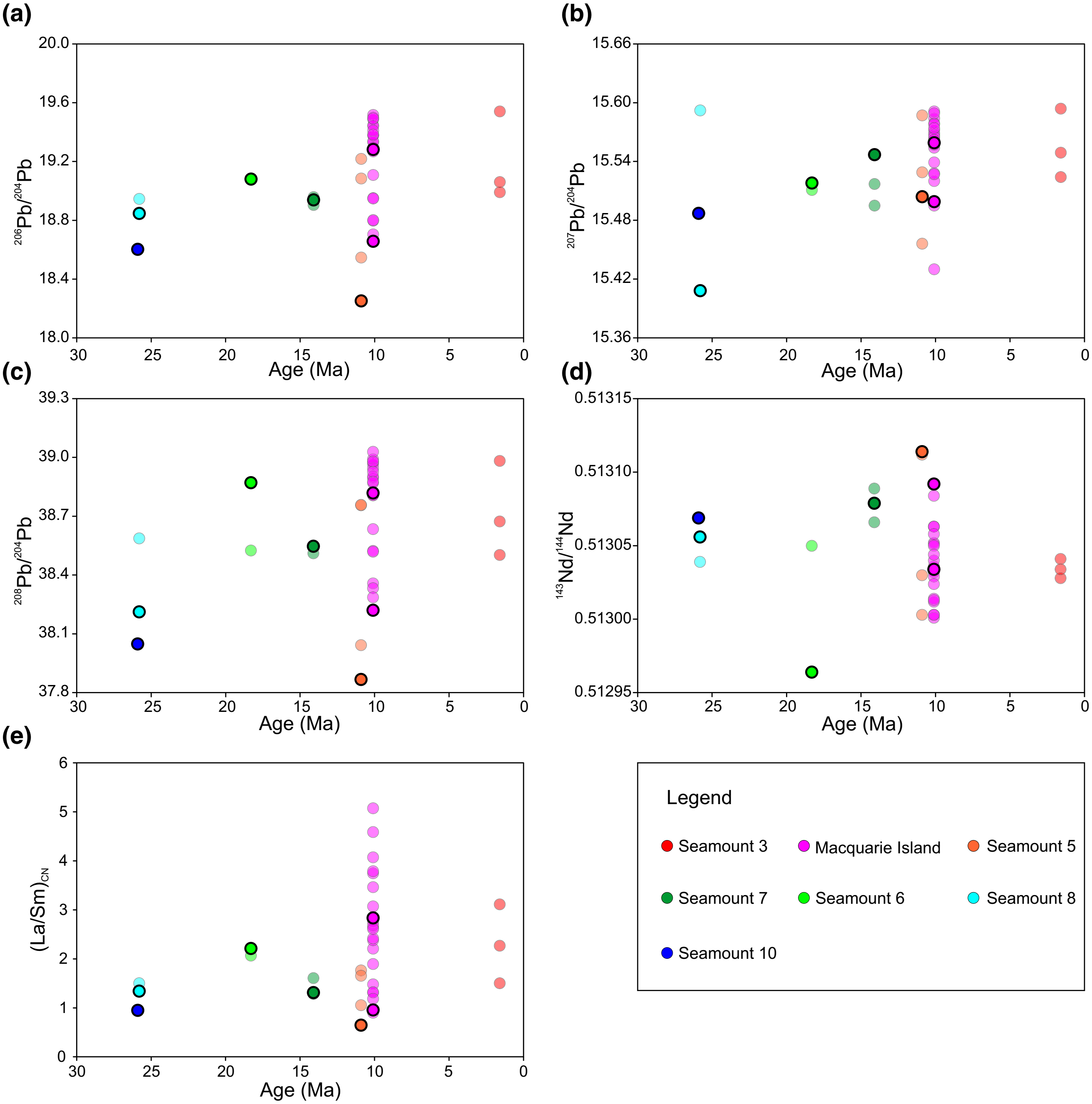

Figure 7. (a) $^{206}Pb/^{204}Pb$, (b) $^{207}Pb/^{204}Pb$, (c) $^{208}Pb/^{204}Pb$, (d) $^{143}Nd/^{144}Nd$, and (e) $(La/Sm)_{CN}$ ratios versus ages for the Macquarie Ridge Complex samples. The isotope data are plotted using the same age for each seamount/island. Symbols with thick boundary represent samples with good age constraints, and the other samples are represented by semi-transparent symbols. The La/Sm ratios are normalized to C1 chondrite (Sun & McDonough, 1989). The isotope data are filtered for loss-on-ignition (LOI < 2.5%) and can be found in Table S4.

degree of partial melting is low during the gradual slowdown and dying of seafloor spreading and decline of spreading-related magmatism (e.g., Dick, 1989; Michael & Cornell, 1998). Under these conditions, the easily fusible and enriched mantle components are preferentially melted and sampled. However, at normal spreading mid-ocean ridges, the degree of partial melting is relatively high, so, even if a small amount of enriched component exists within the upper mantle at this location, the enriched mantle signature would be overwhelmed by dilution by the depleted component. This implies that the upper asthenospheric mantle

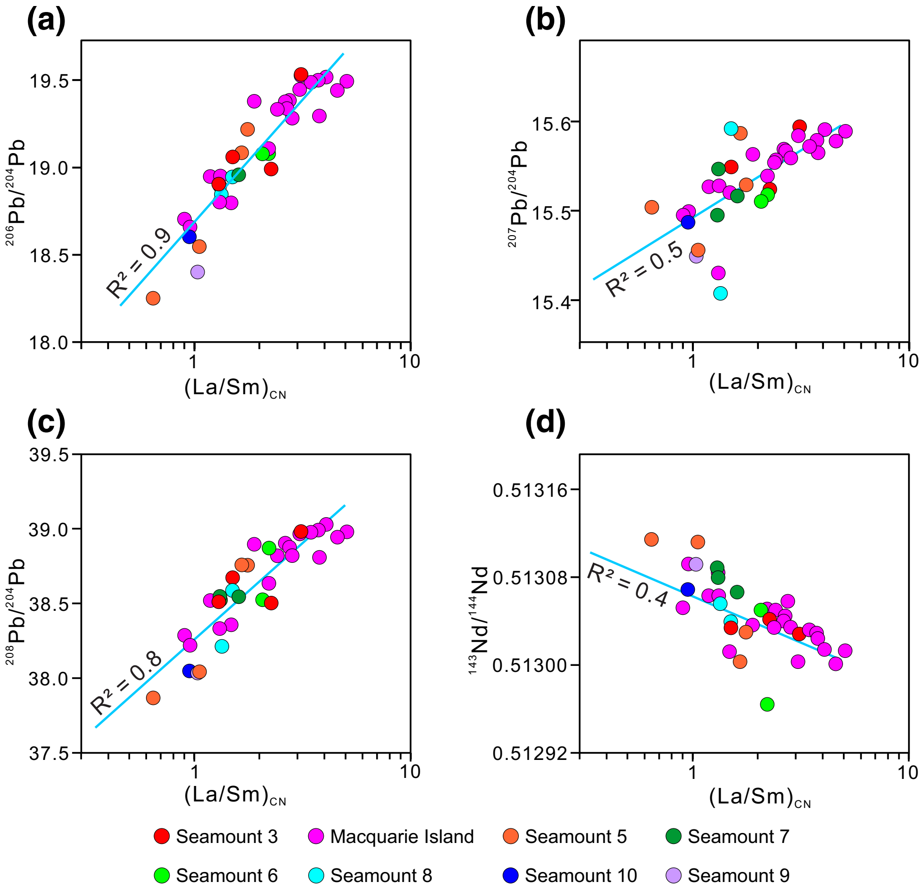

Figure 8. (a) ^{206}Pb/^{204}Pb, (b) ^{207}Pb/^{204}Pb, (c) ^{208}Pb/^{204}Pb, and (d) ^{143}Nd/^{144}Nd ratios versus (La/Sm)$_{CN}$ for the Macquarie Ridge Complex basalts. The blue lines indicate liner regressions. The La/Sm ratios are normalized to C1 chondrite (Sun & McDonough, 1989). The isotope and rare earth element data are filtered for loss-on-ignition (LOI < 2.5%) and can be found in Table S4.

source for MORB is actually quite heterogeneous and could contain a certain amount of "invisible" enriched component, which is in contrast with the commonly accepted view that the mantle source of MORB have been depleted by melt extraction and homogenized by convective stirring (e.g., Salters & Stracke, 2004; Zindler & Hart, 1986). This is in agreement with an increasing number of publications demonstrating the chemical heterogeneity for the mantle source of MORB (e.g., Brunelli et al., 2018; Cousens et al., 2017; Dosso et al., 1993; Liu & Liang, 2017). This heterogeneity is revealed when seafloor spreading slows and ceases, as at the Macquarie Ridge. Although caution should be exercised for a direct analogy between the Macquarie Ridge and other normal mid-ocean ridges, as the Macquarie Ridge was a relatively short-lived proto-mid-ocean ridge and probably did not have as much chance of depletion of the asthenosphere and convective mixing as other mid-ocean ridges.

7. Conclusions

New ^{40}Ar/^{39}Ar and U–Pb ages show that basalts from the Macquarie Ridge Complex seamounts were formed at 25.90 ± 0.23 Ma to 1.59 ± 0.26 Ma and at ~10 Ma from Macquarie Island. The new ages and plate reconstruction results indicate that the cessation of seafloor spreading at the proto-Macquarie mid-ocean ridge generally propagated from south to north along the ridge. The age data and isotopic ratios of the MRC basalts suggest that basalts produced by the proto-Macquarie mid-ocean ridge at different ages on different seamounts and Macquarie Island show no clear covariation between ages and isotopic ratios. The heterogeneous isotopic signatures of MORBs produced by dying mid-ocean ridges indicate that the upper asthenospheric mantle is highly heterogeneous.

Data Availability Statement

All data in this study are available in the Supporting Information and are archived in the Australian Antarctic Data Center (https://data.aad.gov.au/; https://doi.org/10.26179/5d9fbfdea577b).

Acknowledgment
The authors are grateful to the financial support from the Australian Antarctic Division Science Project #4444 and the Polar Rock Repository for providing four dredge samples for this study. The authors thank the AAD staff at the Kensington headquarters and on Macquarie Island for support in managing the project, organizing the field trip and logistics. The authors are particularly thankful for support in the field from safety officer M. Raymond, ranger A. Turbett and station leader K. Williams. C. Mayers, A. Frew, and Z. Martelli from the Western Australian Argon Isotope Facility are thanked for help in sample preparation and analysis. Jiang acknowledges the support of the CSC-CIPRS scholarship. This is NordSIMS publication # 663. Helpful comments by A. Marzoli, K. Konrad, and K. Haase, and editorial handling by J. Blichert-Toft are gratefully acknowledged.

References

Baksi, A. K. (2007). A quantitative tool for evaluating alteration in undisturbed rocks and minerals—I: Water, chemical weathering and atmospheric argon. In G. R. Foulger, & D. M. Jurdy (Eds.), *Plates, plumes, and planetary processes* (pp. 285–303). Geological Society of America Special Papers. https://doi.org/10.1130/2007.2430

Batiza, R., & Vanko, D. A. (1985). Petrologic evolution of large failed rifts in the eastern Pacific: Petrology of volcanic and plutonic rocks from the Mathematician Ridge area and the Guadalupe Trough. *Journal of Petrology*, *26*(3), 564–602. https://doi.org/10.1093/petrology/26.3.564

Bohrson, W. A., Reid, M. R., Grunder, A. L., Heizler, M. T., Harrison, T. M., & Lee, J. (1996). Prolonged history of silicic peralkaline volcanism in the eastern Pacific Ocean. *Journal of Geophysical Research*, *101*(B5), 11457–11474. https://doi.org/10.1029/96JB00329

Brunelli, D., Cipriani, A., & Bonatti, E. (2018). Thermal effects of pyroxenites on mantle melting below mid-ocean ridges. *Nature Geoscience*, *11*(7), 520–525. https://doi.org/10.1038/s41561-018-0139-z

Castillo, P., Clague, D., Davis, A., & Lonsdale, P. (2010). Petrogenesis of Davidson Seamount lavas and its implications for fossil spreading center and intraplate magmatism in the eastern Pacific. *Geochemistry, Geophysics Geosystems*, *11*(2), Q02005. https://doi.org/10.1029/2009GC002992

Choe, W. H., Lee, J. I., Lee, M. J., Do Hur, S., & Jin, Y. K. (2007). Origin of E-MORB in a fossil spreading center: The Antarctic-Phoenix Ridge, Drake Passage, Antarctica. *Geoscience Journal*, *11*(3), 185. https://doi.org/10.1007/BF02913932

Choi, S. H., Choe, W. H., & Lee, J. I. (2008). Mantle heterogeneity beneath the Antarctic–Phoenix ridge off Antarctic Peninsula. *Island Arc*, *17*(1), 172–182. https://doi.org/10.1111/j.1440-1738.2007.00609.x

Choi, S. H., Schiano, P., Chen, Y., Devidal, J.-L., Choo, M. K., & Lee, J.-I. (2013). Melt inclusions in olivine and plagioclase phenocrysts from Antarctic–Phoenix Ridge basalts: Implications for origins of N-and E-type MORB parent magmas. *Journal of Volcanology and Geothermal Research*, *253*, 75–86. https://doi.org/10.1016/j.jvolgeores.2012.12.008

Conway, C. E., Bostock, H. C., Baker, J. A., Wysoczanski, R. J., & Verdier, A. L. (2012). Evolution of Macquarie Ridge Complex seamounts: Implications for volcanic and tectonic processes at the Australia-Pacific plate boundary south of New Zealand. *Marine Geology*, *295*, 34–50. https://doi.org/10.1016/j.margeo.2011.11.009

Cousens, B., Weis, D., Constantin, M., & Scott, S. (2017). Radiogenic isotopes in enriched mid-ocean ridge basalts from Explorer Ridge, northeast Pacific Ocean. *Geochimica et Cosmochimica Acta*, *213*, 63–90. https://doi.org/10.1016/j.gca.2017.06.032

Crisp, J. A. (1984). Rates of magma emplacement and volcanic output. *Journal of Volcanology and Geothermal Research*, *20*(3–4), 177–211. https://doi.org/10.1016/0377-0273(84)90039-8

Davis, A., Clague, D., Cousens, B., Keaten, R., & Paduan, J. (2008). Geochemistry of basalt from the North Gorda segment of the Gorda Ridge: Evolution toward ultraslow spreading ridge lavas due to decreasing magma supply. *Geochemistry, Geophysics, Geosystems*, *9*(4). https://doi.org/10.1029/2007GC001775

Davis, A., Clague, D., Paduan, J., Cousens, B., & Huard, J. (2010). Origin of volcanic seamounts at the continental margin of California related to changes in plate margins. *Geochemistry, Geophysics, Geosystems*, *11*(5). https://doi.org/10.1029/2010GC003064

Dick, H. J. B. (1989). Abyssal peridotites, very slow spreading ridges and ocean ridge magmatism. *Geological Society–Special Publications*, *42*(1), 71–105. https://doi.org/10.1144/GSL.SP.1989.042.01.06

Dijkstra, A. H., Sergeev, D. S., Spandler, C., Pettke, T., Meisel, T., & Cawood, P. A. (2010). Highly refractory peridotites on Macquarie Island and the case for anciently depleted domains in the Earth's mantle. *Journal of Petrology*, *51*(1–2), 469–493. https://doi.org/10.1093/petrology/egp084

Dosso, L., Bougault, H., & Joron, J.-L. (1993). Geochemical morphology of the North Mid-Atlantic Ridge, 10°–24°N: Trace element-isotope complementarity. *Earth Planetary Science Letters*, *120*(3–4), 443–462. https://doi.org/10.1016/0012-821X(93)90256-9

Duncan, R. A., & Hogan, L. G. (1994). Radiometric dating of young MORB Using the ^{40}Ar-^{39}Ar incremental heating method. *Geophysical Research Letters*, *21*(18), 1927–1930. https://doi.org/10.1029/94GL01375

Duncan, R. A., & Varne, R. (1988). The age and distribution of the igneous rocks of Macquarie Island. *Papers and Proceedings of the Royal Society of Tasmania*, *122*(1), 45–50. https://doi.org/10.26749/rstpp.122.1.45

Goscombe, B. D., & Everard, J. L. (1998). *1:10,000 Geological map of Macquarie Island, series of 7 maps*. Mineral Resources Tasmania.

Grimes, C. B., Ushikubo, T., Kozdon, R., & Valley, J. W. (2013). Perspectives on the origin of plagiogranite in ophiolites from oxygen isotopes in zircon. *Lithos*, *179*, 48–66. https://doi.org/10.1016/j.lithos.2013.07.026

Haase, K. M., Beier, C., Fretzdorff, S., Leat, P. T., Livermore, R., Barry, T., et al. (2011). Magmatic evolution of a dying spreading axis: Evidence for the interaction of tectonics and mantle heterogeneity from the fossil Phoenix Ridge Drake Passage. *Chemical Geology*, *280*(1–2), 115–125. https://doi.org/10.1016/j.chemgeo.2010.11.002

Haase, K. M., Devey, C. W., Mertz, D. F., Stoffers, P., & Garbe-Schönberg, D. (1996). Geochemistry of lavas from Mohns Ridge, Norwegian-Greenland Sea: Implications for melting conditions and magma sources near Jan Mayen. *Contributions to Mineralogy and Petrology*, *123*(3), 223–237. https://doi.org/10.1007/s004100050152

Haase, K. M., Regelous, M., Duncan, R. A., Brandl, P. A., Stroncik, N., & Grevemeyer, I. (2011). Insights into mantle composition and mantle melting beneath mid-ocean ridges from postspreading volcanism on the fossil Galapagos Rise. *Geochemistry, Geophysics, Geosystems*, *12*(5). https://doi.org/10.1029/2010GC003482

Hofmann, C., Feraud, G., & Courtillot, V. (2000). ^{40}Ar/^{39}Ar dating of mineral separates and whole rocks from the Western Ghats lava pile: Further constraints on duration and age of the Deccan traps. *Earth and Planetary Science Letters*, *180*(1–2), 13–27. https://doi.org/10.1016/S0012-821x(00)00159-X

Jiang, Q., Merle, R. E., Jourdan, F., Olierook, H. K. H., Chiaradia, M., Evans, K. A., et al. (2020). Origin of geochemically heterogeneous mid-ocean ridge basalts from the Macquarie Ridge Complex, SW Pacific. *Lithos*, 105893. https://doi.org/10.1016/j.lithos.2020.105893

Jourdan, F., Feraud, G., Bertrand, H., Watkeys, M., & Renne, P. R. (2007). Distinct brief major events in the Karoo large igneous province clarified by new ^{40}Ar/^{39}Ar ages on the Lesotho basalts. *Lithos*, *98*(1–4), 195–209. https://doi.org/10.1016/j.lithos.2007.03.002

Jourdan, F., Reimold, W. U., & Deutsch, A. (2012). Dating terrestrial impact structures. *Elements*, *8*(1), 49–53. https://doi.org/10.2113/gselements.8.1.49

Jourdan, F., & Renne, P. R. (2007). Age calibration of the Fish Canyon sanidine ^{40}Ar/^{39}Ar dating standard using primary K-Ar standards. *Geochimica et Cosmochimica Acta*, *71*(2), 387–402. https://doi.org/10.1016/j.gca.2006.09.002

Jourdan, F., Timms, N. E., Eroglu, E., Mayers, C., Frew, A., Bland, P., et al. (2017). Collisional history of asteroid Itokawa. *Geology*, *45*(9), 819–822. https://doi.org/10.1130/G39138.1

Kamenetsky, V. S., Everard, J. L., Crawford, A. J., Varne, R., Eggins, S. M., & Lanyon, R. (2000). Enriched end-member of primitive MORB melts: Petrology and geochemistry of glasses from Macquarie Island (SW Pacific). *Journal of Petrology*, *41*(3), 411–430. https://doi.org/10.1093/petrology/41.3.411

Kamenetsky, V. S., & Maas, R. (2002). Mantle-melt evolution (dynamic source) in the origin of a single MORB suite: A perspective from magnesian glasses of Macquarie Island. *Journal of Petrology*, *43*(10), 1909–1922. https://doi.org/10.1093/petrology/43.10.1909

Keller, W. R. (2004). *Cenozoic plate tectonic reconstructions and plate boundary processes in the Southwest Pacific*, (PhD thesis). Pasadena, CA: California Institute of Technology.

Kennedy, T., Jourdan, F., Eroglu, E., & Mayers, C. (2019). Bombardment history of asteroid 4 Vesta recorded by brecciated eucrites: Large impact event clusters at 4.50 Ga and discreet bombardment until 3.47 Ga. *Geochimica et Cosmochimica Acta*, *260*, 99–123. https://doi.org/10.1016/j.gca.2019.06.027

Koppers, A. A. P. (2002). ArArCALC—software for ^{40}Ar/^{39}Ar age calculations. *Computational Geosciences*, *28*(5), 605–619. https://doi.org/10.1016/S0098-3004(01)00095-4

Lamarche, G., Collot, J. Y., Wood, R. A., Sosson, M., Sutherland, R., & Delteil, J. (1997). The Oligocene-Miocene Pacific-Australia plate boundary, south of New Zealand: Evolution from oceanic spreading to strike-slip faulting. *Earth and Planetary Science Letters*, *148*(1–2), 129–139. https://doi.org/10.1016/S0012-821x(97)00026-5

Lebrun, J. F., Lamarche, G., & Collot, J. Y. (2003). Subduction initiation at a strike-slip plate boundary: The Cenozoic Pacific-Australian plate boundary, south of New Zealand. *Journal of Geophysical Research*, *108*(B9). https://doi.org/10.1029/2002JB002041

Lee, J. Y., Marti, K., Severinghaus, J. P., Kawamura, K., Yoo, H. S., Lee, J. B., & Kim, J. S. (2006). A redetermination of the isotopic abundances of atmospheric Ar. *Geochimica et Cosmochimica Acta*, *70*(17), 4507–4512. https://doi.org/10.1016/j.gca.2006.06.1563

Li, X. H., Long, W. G., Li, Q. L., Liu, Y., Zheng, Y. F., Yang, Y. H., et al. (2010). Penglai zircon megacrysts: A potential new working reference material for microbeam determination of Hf–O isotopes and U–Pb age. *Geostandards and Geoanalytical Research*, *34*(2), 117–134. https://doi.org/10.1111/j.1751-908X.2010.00036.x

Liu, B., & Liang, Y. (2017). The prevalence of kilometer-scale heterogeneity in the source region of MORB upper mantle. *Science Advances*, *3*(11), e1701872. https://doi.org/10.1126/sciadv.1701872

Ludwig, K. (2008). *Isoplot version 4.15: A geochronological toolkit for microsoft excel*. Berkeley Geochronology Center, Special Publication.

MacLeod, S. J., Williams, S. E., Matthews, K. J., Müller, R. D., & Qin, X. (2017). A global review and digital database of large-scale extinct spreading centers. *Geosphere*, *13*(3), 911–949. https://doi.org/10.1130/GES01379.1

Massell, C., Coffin, M. F., Mann, P., Mosher, S., Frohlich, C., Duncan, C. S., et al. (2000). Neotectonics of the Macquarie Ridge Complex, Australia-Pacific plate boundary. *Journal of Geophysical Research*, *105*(B6), 13457–13480. https://doi.org/10.1029/1999jb900408

Meckel, T. A., Coffin, M. F., Mosher, S., Symonds, P., Bernardel, G., & Mann, P. (2003). Underthrusting at the Hjort Trench, Australian-Pacific plate boundary: Incipient subduction? *Geochemistry, Geophysics, Geosystems*, *4*. https://doi.org/10.1029/2002GC000498

Meckel, T. A., Mann, P., Mosher, S., & Coffin, M. F. (2005). Influence of cumulative convergence on lithospheric thrust fault development and topography along the Australian-Pacific plate boundary south of New Zealand. *Geochemistry, Geophysics, Geosystems*, *6*. https://doi.org/10.1029/2005gc000914

Merle, R. E., Jourdan, F., Chiaradia, M., Olierook, H. K. H., & Manatschal, G. (2019). Origin of widespread Cretaceous alkaline magmatism in the Central Atlantic: A single melting anomaly? *Lithos*, *342*, 480–498. https://doi.org/10.1016/j.lithos.2019.06.002

Michael, P. J., & Cornell, W. C. (1998). Influence of spreading rate and magma supply on crystallization and assimilation beneath mid-ocean ridges: Evidence from chlorine and major element chemistry of mid-ocean ridge basalts. *Journal of Geophysical Research*, *103*(B8), 18325–18356. https://doi.org/10.1029/98JB00791

Mosher, S., & Symons, C. M. (2008). Ridge reorientation mechanisms: Macquarie ridge complex, Australia-Pacific plate boundary. *Geology*, *36*(2), 119–122. https://doi.org/10.1130/G24236a.1

Mühe, R., Bohrmann, H., Garbe-Schönberg, D., & Kassens, H. (1997). E-MORB glasses from the Gakkel Ridge (Arctic Ocean) at 87°N: Evidence for the Earth's most northerly volcanic activity. *Earth and Planetary Science Letters*, *152*(1–4), 1–9. https://doi.org/10.1016/S0012-821X(97)00152-0

Nasdala, L., Hofmeister, W., Norberg, N., Martinson, J. M., Corfu, F., Dörr, W., et al. (2008). Zircon M257-a homogeneous natural reference material for the ion microprobe U-Pb analysis of zircon. *Geostandards and Geoanalytical Research*, *32*(3), 247–265. https://doi.org/10.1111/j.1751-908X.2008.00914.x

Neumann, E.-R., & Schilling, J.-G. (1984). Petrology of basalts from the Mohns-Knipovich ridge; the Norwegian-Greenland Sea. *Contributions to Mineralogy and Petrology*, *85*(3), 209–223. https://doi.org/10.1007/BF00378101

Olierook, H. K. H., Jiang, Q., Jourdan, F., & Chiaradia, M. (2019). Greater Kerguelen large igneous province reveals no role for Kerguelen mantle plume in the continental breakup of eastern Gondwana. *Earth and Planetary Science Letters*, *511*, 244–255. https://doi.org/10.1016/j.epsl.2019.01.037

Olierook, H. K. H., Merle, R. E., & Jourdan, F. (2017). Toward a Greater Kerguelen large igneous province: Evolving mantle source contributions in and around the Indian Ocean. *Lithos*, *282*, 163–172. https://doi.org/10.1016/j.lithos.2017.03.007

Oostingh, K. F., Jourdan, F., Matchan, E. L., & Phillips, D. (2017). ^{40}Ar/^{39}Ar geochronology reveals rapid change from plume-assisted to stress-dependent volcanism in the Newer Volcanic Province, SE Australia. *Geochemistry, Geophysics, Geosystems*, *18*(3), 1065–1089. https://doi.org/10.1002/2016GC006601

Renne, P. R., Balco, G., Ludwig, K. R., Mundil, R., & Min, K. (2011). Joint determination of 40K decay constants and 40Ar*/40K for the Fish Canyon sanidine standard, and improved accuracy for 40Ar/39Ar geochronology. *Geochimica et Cosmochimica Acta*, *75*(17), 5097–5100. https://doi.org/10.1016/j.gca.2011.06.021

Renne, P. R., Deino, A. L., Hilgen, F. J., Kuiper, K. F., Mark, D. F., Mitchell, W. S., et al. (2013). Time scales of critical events around the Cretaceous-Paleogene Boundary. *Science*, *339*(6120), 684–687. https://doi.org/10.1126/science.1230492

Renne, P. R., Mundil, R., Balco, G., Min, K., & Ludwig, K. R. (2010). Joint determination of ^{40}K decay constants and ^{40}Ar*/^{40}K for the Fish Canyon sanidine standard, and improved accuracy for ^{40}Ar/^{39}Ar geochronology. *Geochimica et Cosmochimica Acta*, *74*(18), 5349–5367. https://doi.org/10.1016/j.gca.2010.06.017

Renne, P. R., Sprain, C. J., Richards, M. A., Self, S., Vanderkluysen, L., & Pande, K. (2015). State shift in Deccan volcanism at the Cretaceous-Paleogene boundary, possibly induced by impact. *Science*, *350*(6256), 76–78. https://doi.org/10.1126/science.aac7549

Renne, P. R., Swisher, C. C., Deino, A. L., Karner, D. B., Owens, T. L., & DePaolo, D. J. (1998). Intercalibration of standards, absolute ages and uncertainties in ^{40}Ar/^{39}Ar dating. *Chemical Geology*, *145*(1–2), 117–152. https://doi.org/10.1016/S0009-2541(97)00159-9

Ryan, W. B. F., Carbotte, S. M., Coplan, J. O., O'Hara, S., Melkonian, A., Arko, R., et al. (2009). Global multi-resolution topography synthesis. *Geochemistry, Geophysics, Geosystems*, *10*. https://doi.org/10.1029/2008gc002332

Salters, V. J. M., & Stracke, A. (2004). Composition of the depleted mantle. *Geochemistry, Geophysics, Geosystems*, *5*. https://doi.org/10.1029/2003gc000597

Schaen, A. J., Jicha, B. R., Hodges, K. V., Vermeesch, P., Stelten, M. E., Mercer, C. M., et al. (2020). Interpreting and reporting ^{40}Ar/^{39}Ar geochronologic data. *The Geological Society of America Bulletin*. https://doi.org/10.1130/B35560.1

Seton, M., Müller, R. D., Zahirovic, S., Gaina, C., Torsvik, T. H., Shephard, G., et al. (2012). Global continental and ocean basin reconstructions since 200 Ma. *Earth-Science Reviews*, *113*(3–4), 212–270. https://doi.org/10.1016/j.earscirev.2012.03.002

Stacey, J. S., & Kramers, J. D. (1975). Approximation of terrestrial lead isotope evolution by a two-stage model. *Earth and Planetary Science Letters*, *26*(2), 207–221. https://doi.org/10.1016/0012-821X(75)90088-6

Standish, J. J., Dick, H. J., Michael, P. J., Melson, W. G., & O'Hearn, T. (2008). MORB generation beneath the ultraslow spreading Southwest Indian Ridge (9–25°E): Major element chemistry and the importance of process versus source. *Geochemistry, Geophysics, Geosystems*, *9*(5). https://doi.org/10.1029/2008GC001959

Sun, S.-S., & McDonough, W. F. (1989). Chemical and isotopic systematics of oceanic basalts: Implications for mantle composition and processes. *Geological Society - Special Publications*, *42*(1), 313–345. https://doi.org/10.1144/GSL.SP.1989.042.01.19

Sutherland, R. (1995). The Australia-Pacific boundary and Cenozoic plate motions in the SW Pacific: Some constraints from Geosat data. *Tectonics*, *14*(4), 819–831. https://doi.org/10.1029/95TC00930

Tian, L., Castillo, P. R., Lonsdale, P. F., Hahm, D., & Hilton, D. R. (2011). Petrology and Sr-Nd-Pb-He isotope geochemistry of post spreading lavas on fossil spreading axes off Baja California Sur, Mexico. *Geochemical Geophysical Geosystems*, *12*(2), Q0AC10. https://doi.org/10.1029/2010GC003319

Valley, J. W., Kinny, P. D., Schulze, D. J., & Spicuzza, M. J. (1998). Zircon megacrysts from kimberlite: Oxygen isotope variability among mantle melts. *Contributions to Mineralogy and Petrology*, *133*(1–2), 1–11. https://doi.org/10.1007/s004100050432

Varne, R., Brown, A. V., & Falloon, T. (2000). Macquarie Island: Its geology, structural history, and the timing and tectonic setting of its N-MORB to E-MORB magmatism. *Geological Society of America Special Paper*, *349*, 301–320. https://doi.org/10.1130/0-8137-2349-3.301

Verati, C., & Jourdan, F. (2014). Modeling effect of sericitization of plagioclase on the ^{40}K/^{40}Ar and ^{40}Ar/^{39}Ar chronometers: Implication for dating basaltic rocks and mineral deposits. *Geological Society - Special Publications*, *378*(1), 155–174. https://doi.org/10.1144/SP378.14

Ware, B., & Jourdan, F. (2018). ^{40}Ar/^{39}Ar geochronology of terrestrial pyroxene. *Geochimica et Cosmochimica Acta*, *230*, 112–136. https://doi.org/10.1016/j.gca.2018.04.002

Wertz, K. L. (2003). *From seafloor spreading to uplift: The structural and geochemical evolution of Macquarie island on the Australian-Pacific plate boundary* (Doctoral dissertation). Austin, TX: The University of Texas at Austin.

Wiedenbeck, M., Hanchar, J. M., Peck, W. H., Sylvester, P., Valley, J., Whitehouse, M., et al. (2004). Further characterization of the 91500 zircon crystal. *Geostandards and Geoanalytical Research*, *28*(1), 9–39. https://doi.org/10.1111/j.1751-908X.2004.tb01041.x

Wood, R., Lamarche, G., Herzer, R., Delteil, J., & Davy, B. (1996). Paleogene seafloor spreading in the southeast Tasman sea. *Tectonics*, *15*(5), 966–975. https://doi.org/10.1029/96tc00129

Zindler, A., & Hart, S. (1986). Chemical geodynamics. *Advanced Refractive Effects Prediction System*, *14*, 493–571. https://doi.org/10.1146/annurev.ea.14.050186.002425